TECHNISCHE
UNIVERSITÄT
WIEN
Vienna University of Technology

INSTITUT FÜR
MECHANIK UND
MECHATRONIK
Mechanics & Mechatronics

DIPLOMARBEIT

Moving Horizon State Estimation for a PEM Fuel Cell System based on Successive Linearisation

ausgeführt zum Zwecke der Erlangung des akademischen Grades eines Diplom-Ingenieurs
unter der Betreuung von

Dr. Lukas Böhler

und unter der Leitung von

Univ.Prof. Dr. Stefan Jakubek
Institut für Mechanik und Mechatronik
Abteilung für Regelungstechnik und Prozessautomatisierung

eingereicht an der Technischen Universität Wien

Fakultät für Maschinenwesen und Betriebswissenschaften

von

Michael Lehner
Matr.Nr.: 01427146
[redacted]

Eidesstattliche Erklärung

Ich erkläre eidesstattlich, dass ich die Arbeit selbständig angefertigt, keine anderen als die angegebenen Hilfsmittel benutzt und alle aus ungedruckten Quellen, gedruckter Literatur oder aus dem Internet im Wortlaut oder im wesentlichen Inhalt übernommenen Formulierungen und Konzepte gemäß den Richtlinien wissenschaftlicher Arbeiten zitiert, durch Fußnoten gekennzeichnet bzw. mit genauer Quellenangabe kenntlich gemacht habe.

Wien, am 13. Oktober 2021 Michael Lehner

Danksagung

Leider lässt sich eine wahrhafte Dankbarkeit mit Worten nicht ausdrücken.

Johann Wolfgang von Goethe (1749-1832)

Kurzfassung

Aufgrund der starken Nachfrage nach nachhaltigen und umweltfreundlichen Energiequellen, ist die Brennstoffzelle wieder in Fokus der Wissenschaft geraten. Wird die Brennstoffzelle mit grünem Wasserstoff betrieben, so stellt sie eine vollständig CO_2-neutrale Alternative zu den konventionellen Energieerzeugungsmethoden dar. Eine große Herausforderung beim Betrieb der Brennstoffzelle ist, dass sie sensibel auf bestimmte Betriebsschwankungen und Störungen reagiert. Um einen effizienten und zuverlässigen Betrieb einer Polymerelektrolyt-Membran Brennstoffzelle (PEM) gewährleisten zu können, muss der Zustand der Brennstoffzelle ständig überwacht werden. Da die internen relevanten Zustände nicht gemessen werden können, müssen diese mit Hilfe eines Zustandsbeobachter rekonstruiert werden. Diese Arbeit befasst sich mit der Entwicklung und Implementierung eines Zustandsschätzers auf bewegtem Horizont (engl. *moving horizon estimation*, MHE) für ein PEM Brennstoffzellenmodell. Zuerst wird ein nulldimensionales Modell der Brennstoffzelle erstellt, welches die wesentlichen Effekte enthält und das grundlegende Systemverhalten abbildet. Anschließend wird eine Formulierung des MHEs auf Basis der sukzessiven Linearisierung hergleitet, welche eine Umsetzung des Beobachterkonzeptes mit gängigen quadratischen Solvern ermöglicht. Die Validierung der Zustandsschätzmethode erfolgt auf dem PEM Brennstoffzellenmodell und dem 3-Tank Modell, die beide nichtlineare Systeme darstellen. Abschließend werden verschiedene Eigenschaften des MHEs näher analysiert und der Beobachter wird mit einem extended Kalman Filter (EKF) verglichen. Die Simulationsergebnisse zeigen, dass der MHE auf Basis der sukzessiven Linearisierung die Zustände auf beiden Systemen mit einer zufriedenstellenden Genauigkeit beobachten kann. Weiters zeigen die Untersuchungen, dass die hergeleitete Formulierung des Beobachters ausreichend genau ist und dieser auch zur Rekonstruktion des Anfangszustandes bei einer fehlerhaften initialen Schätzung geeignet ist. Der hergeleitete MHE überzeugt durch seine Konvergenzeigenschaften und die vorteilhafte matrixbasierte Formulierung.

Abstract

Due to the growing demand for sustainable and environmentally friendly energy sources, the fuel cell has become the focus of science once again. If the fuel cell is operated with green hydrogen, it represents an entirely CO_2-neutral alternative to conventional energy generation methods. A major challenge in the operation of the fuel cell is that it is sensitive to certain conditions and disturbances. In order to ensure efficient and reliable operation of a polymer electrolyte membrane fuel cell (PEMFC), the condition of the fuel cell has to be monitored. Since the relevant internal states cannot be measured, they can be reconstructed, however, with the help of state observers. This thesis deals with developing and implementing a moving horizon estimator (MHE) for a PEM fuel cell model. First, a zero-dimensional model of the fuel cell is developed, which contains the main effects and represents the basic system behaviour. Subsequently, a formulation of the MHE is derived based on successive linearisation, which enables an implementation of the observer concept with common quadratic solvers. The validation of the state estimation method is carried out on the PEM fuel cell model and the 3-tank model, which are both nonlinear systems. Finally, various properties of the MHE are analysed in more detail, and the observer is compared with an extended Kalman filter (EKF). The simulation results show that the MHE can observe the states with satisfactory accuracy based on successive linearisation on both systems. The investigations further show that the derived formulation of the observer is sufficiently accurate and that the MHE can be used to reconstruct the initial state in the case of a poor initial estimation as well. The derived MHE convinces with its convergence properties and the beneficial matrix based formulation.

Contents

List of Figures

List of Tables

Chapter 1

Introduction

Global energy demand is increasing every year. Since, on the one hand, the existing primary energy sources are finite resources and, on the other hand, the increasingly strict regulations regarding CO_2 emissions have to be observed, science, in particular, is called upon to find solutions in the form of sustainable and environmentally friendly energy sources. One promising technology to achieve these goals is the fuel cell. Problems caused by the combustion of fossil fuels, such as air pollution by exhaust gases or fine dust, would be eliminated with this technology. Only water vapour is produced as a reaction product during the combustion of hydrogen in the fuel cell. If, in addition, the hydrogen is produced exclusively through the process of electrolysis with the use of renewable energy, the result is an entirely CO_2-neutral energy source.
Climate targets, such as those of the European Union (EU), which aims to achieve a climate-neutral Europe by 2050 [3], are also driving research forward in the field of fuel cells.
For example, the City of Vienna is not only trying to reach these goals set by the EU, but Austria's federal capital formulates this target even more ambitiously and wants to be CO_2 neutral in all sectors as early as 2040 [4]. An essential part of this plan is the fuel cell and the integration of green hydrogen in the energy sector. In the mobility sector, Vienna wants to gradually switch from buses with conventional diesel engines to hydrogen and battery-powered buses by 2036.
Also for the world's largest automotive supplier Bosch, the mobility of the future will not take place without fuel cells. According to Bosch, the following seven arguments are the reasons for a changing mobility [5]:

- **Neutrality:**
  By using green hydrogen, the fuel cell results in a completely climate-neutral energy source.

- **Potential applications:**
  The field of application is not limited to mobile applications. Fuel cells can also be used in the form of small decentralised power plants in cities, data centres, or charging stations for electric vehicles.

- **Efficiency:**
  Fuel cell vehicles are a quarter more efficient than vehicles with combustion engines [5].

- **Cost:**
  The development, expansion of production capacities, and falling prices for renewable energy for the production of green hydrogen are expected to halve the costs of many hydrogen applications in the next ten years.

- **Infrastructure:**
  The hydrogen refuelling station network is being steadily expanded through government funding programmes.

- **Safety:**
  The use of gaseous hydrogen in vehicles is less dangerous than ordinary other car fuels or batteries. There is also no increased risk of explosion from the tanks.

- **Timing:**
  Both the production of hydrogen is proven and technologically controllable, and the fuel cell has the technological maturity for industrialisation. Thus, through investment and political will, the hydrogen economy becomes competitive in the coming years.

These seven points are reasons why not only Bosch but also many other large manufacturers are investing in the research and development of the fuel cell. A great deal of attention is paid to increasing the service life and ensuring proper operation. This requires constant observation of the fuel cell's health, such as monitoring the membrane humidity. Since, in many cases, it is not possible to measure this condition of the fuel cell, virtual sensors are used. In this work, a method for such a sensor, which is also called a state observer in control engineering, is derived and implemented.

1.1 Motivation

There is still a lot of research to be done before the vision becomes reality that fuel cells will be used in many areas like the automotive industry as a replacement for current

energy sources. A major challenge here is that the cell reacts sensitively to certain operating conditions and disturbances. To ensure the most stable and efficient operation possible, the fuel cell must be constantly monitored. Furthermore, critical operating conditions, such as fuel starvation, membrane flooding or drying, should also be prevented. Since the internal relevant conditions, such as the humidity of the membrane, cannot be measured for technical or constructional reasons, so-called observers are used. An observer replicates the reference system as a model and reconstructs the non-measurable states from known input variables and measured variables of the reference system. The states contain all the information needed to calculate the present or future behaviour of a system without taking the past into account. The accuracy of the state estimator thus also depends on the modeling accuracy, which is, however, limited by the requirement of real-time capability. State estimation minimises the discrepancy between the measured output values of a system and the output values calculated with the reference model. How exactly the minimisation of the difference between the two outputs is done depends on the observer approach.

With the models for the observer, or in general, in model-based control engineering, it is essential to find a model that represents a good compromise between accuracy and computational effort. Low-order models are therefore preferred for these applications. Often the work of Pukrushpan [6] serves as the basis for such models. With a small number of states, the dynamic behaviour of the fuel cell system and all its auxiliary components is described. A model for controlling the hydrogen supply is presented in [7], which also takes anode recirculation and anode bleeding into account. In [8], the transport phenomena of gases and liquid water in the gas diffusion layer are modelled one-dimensionally with the global aim of regulating the air supply system. Furthermore, the model of [6] can be extended in scope and complexity to 16 states to represent the dynamic system behaviour even more precisely [9]. This comprehensive model was extended with effects such as dynamic phase transitions, the transient drying or rewetting of the membrane or the anode gas recirculation. A real-time capable quasi-2D model is presented in [10]. However, this model and models of even higher order are not suitable for applications of model-based control engineering such as observer design due to their increased computational effort. For monitoring the internal conditions, on the one hand, a model is needed that describes the desired effects or states with satisfactory accuracy. On the other hand, a suitable method for reconstructing the internal states must be chosen.

Similar to modelling, there are different methods in the literature for state estimation. One approach is to use the extended Kalman filter [11] for real-time state estimation on a high-order PEM fuel cell system. The EKF is an extension of the Kalman filter

(KF)for nonlinear systems, which updates the linear system matrices of the nonlinear system. Another extension of the Kalman filter for the diagnosis and monitoring of PEM fuel cell conditions is the Unscented Kalman Filter (UKF). The UKF approximates the state distribution by carefully chosen sample points (sigma points) and does not require derivations of the system equations. In [12], the UKF is used for health prognosis and in [13] for control. For fault diagnosis, sliding-mode observer (SMO) approaches are common due to their robustness to disturbances, high accuracy and fast convergence. The nitrogen enrichment on the anode side and the relative humidity in the channels is estimated in [14] using the SMO and in [15] the SMO is applied for fault diagnosis in the air supply system.
Moving horizon estimation [16] is another approach to reconstruct the states of a highly nonlinear system like the fuel cell. The mode of operation of the MHE is similar model predictive control (MPC). For a certain time horizon, which starts in the past and ends at the current time, the initial state of a dynamic system and the disturbances acting on the system are estimated. This estimation is based on maximising the probability of the estimated states under the condition of the measured outputs. At each time step, this maximisation is done in the form of a nonlinear optimisation task [17]. The initial implementation is very time-consuming, and the systematic optimisation process leads to a high computational effort, but the excellent convergence properties of the observer and the applicability for complex nonlinear systems, where the noise signals do not need to have specific stochastic properties, justify this increased implementation effort.
This thesis derives a formulation of the moving horizon estimator based on successive linearisation to obtain an implementation that is as computationally efficient as possible. This formulation of the MHE concept should make it possible to implement the observer with standard quadratic solvers.

This thesis is divided into three chapters. In the first chapter, a model of the PEM fuel cell is created to represent the fundamental relationship between input current and output voltage as a function of the essential internal states. In the second chapter, the formulation of the moving horizon state estimation concept is derived based on successive linearisation. In the third chapter, the observer concept is validated on the highly nonlinear model of the fuel cell, which is a SISO model. To demonstrate that the formulation of the MHE is also applicable to MIMO systems, the MHE is additionally applied to the nonlinear 3-tank system. Since the matrices of the 3-tank model are numerically more tractable, some of the general properties of the MHE for this MIMO system are investigated in more detail.

Chapter 2

Fuel cell modelling

2.1 Introduction to fuel cells

Models are basically used to mathematically represent the essential characteristics of a real system. In model-based control, they form the basis for realising technical challenges, such as the design of an advanced control system, the reconstruction or estimation of system states or fault-detection and diagnosis. However, models of real systems are not only used for control engineering. Modelling and simulation are powerful and valuable tools for investigating complex systems, such as the fuel cell. Important information can be derived from simulation results, which can contribute, for example, to further development of system components or to the understanding of physical phenomena.
How accurate a model has to be, or which effects of the modelled system should be included, always depends on the application. In many areas, such as model-based control, one always has to make an inevitable compromise between accuracy and computational effort.

2.1.1 History of the fuel cell

The fuel cell is a technology that has been researched for some time now. The origins of this energy conversion method go back to the 19th century. However, it is not entirely clear who first discovered the basic principle of the fuel cell. According to [18], the German chemist Christian Friedrich Schönbein was the first to conduct scientific research on the subject of fuel cells in 1838, which he published in 1839. In [19, 20], Sir William Groove is considered the inventor of fuel cell technology, which he first described in 1939. He succeeded in reversing the electrolysis process and building a device that combines hydrogen and oxygen to produce electricity. This device, later known as a fuel cell, was initially called a gas battery. An extremely important insight that

Groove already recognised or discovered is the need for the largest possible contact area between the electrolyte, the gaseous reactants and the electrocatalytic conductor [20]. To increase this active area, Mond and Langers developed in 1889 a three-dimensional porous electrode structure. They were the first to observe the voltage loss due to flooding and that one can increase the voltage output by stacking cells [21]. In 1910, Emil Baur researched the relationship between the output voltage and the current density and was the first to visualize the polarization curve of a fuel cell. Although some researchers like Ostwald were convinced that the 20th century would be the age of electrochemical combustion, it could not prevail against competitors like the steam engine despite its better efficiency and remained a niche product. Francis T. Bacon researched fuel cells as energy storage devices from 1930 onwards. His successes in research led to the fuel cell being used as an energy source in space travel, especially on the Apollo Lunar Mission [21]. The development of the reliable perfluorosulfonic acid proton exchange membrane, Nafion, enables the use of PEM fuel cells in a wide range of applications.
The oil crisis in 1973, increasingly strict emission laws and the growing demand for alternative technologies independent of fossil fuels have driven the further development of fuel cells in recent decades. The following aspects characterised the subsequent decades of development: Removal of diffusion restrictions in the electrodes to increase efficiency, reduction in the cost of catalysts, increase in performance and service life.

2.1.2 Basics of the fuel cell

The fuel cell is an energy converter that transforms chemical energy into electrical energy. A significant difference to other processes for obtaining electrical power from chemical energy is the number of energy transformations. Figure 2.1 shows the comparison of the energy conversions of an internal combustion engine and the fuel cell. When fossil fuels are turned into electricity, the chemically bound energy is changed into heat energy in the first step by burning the fuel. This released heat is now converted into mechanical work. Typically this is done by using the heat energy to boil water and drive a turbine with the generated water steam. In the final step, electricity is made out of mechanical energy using a generator. The fuel cell bypasses all these steps and converts the energy from chemical to electrical energy in just one step, resulting in better efficiency. One can therefore compare the fuel cell with a battery. In both forms of energy generation, chemical bounded energy is converted directly into electrical energy. The main difference between the two energy sources is that the fuel cell generates energy as long as fuel is supplied and does not consume itself in generating electrical power, as a battery does, for example.

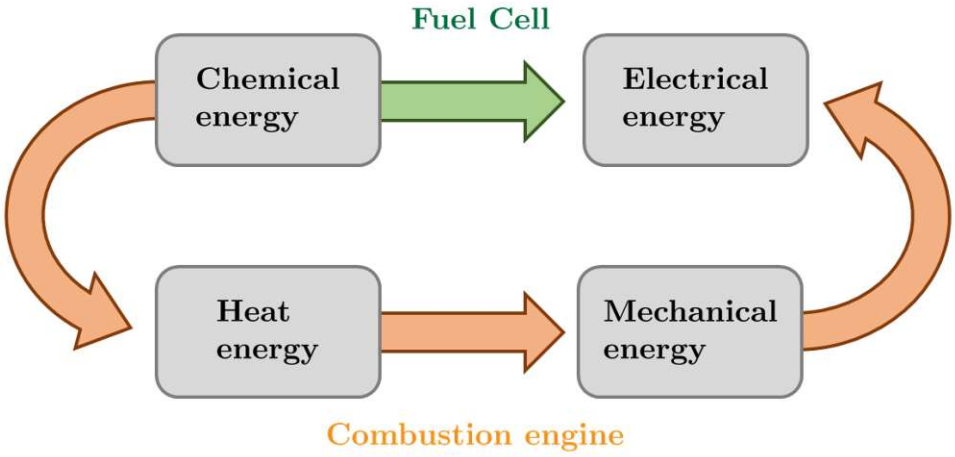

Figure 2.1: Schematic comparison of the energy conversions of a fuel cell and the combustion engine [1].

The fuel cell generates electrical energy from pure hydrogen and oxygen, which is usually provided from the ambient air. The principle of action is based on the combustion of hydrogen

$$H_2 + \frac{1}{2} O_2 \rightleftarrows H_2O. \tag{2.1}$$

When the two molecules, hydrogen H_2 and oxygen O_2 react with each other, the reaction product is water, which has lower bonding energy than the initial products. If this reaction takes place in an uncontrolled manner, the energy difference, as seen in Figure 2.2, is released in the form of heat.

Breaking of the H_2 and O_2 molecules and the reconfiguration of the H_2O bonds occurs through an electron exchange. The difference in the bonding energy of the initial molecules and the reaction product, which can be seen in Figure 2.2, results from this electron transfer and reconfiguration. If this reaction proceeds uncontrolled, the released energy can only be gained in the form of heat since the electron transfer takes place within a few picoseconds. Thus, it would again take more than one transformation step to generate electrical energy.

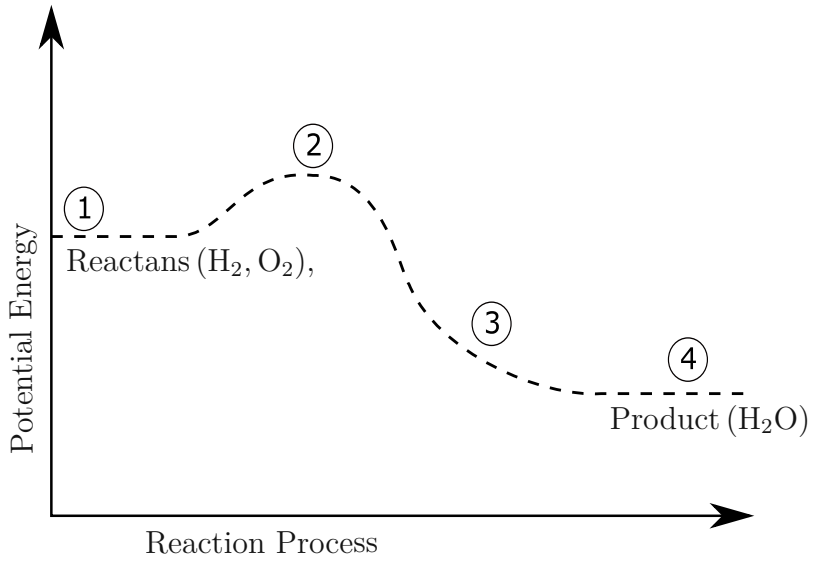

Figure 2.2: Schematic of H_2 - O_2 reaction [1]. (1) Starting with H_2 - O_2 gases. (2) bonds must be broken up, requiring energy input. (3,4) Hydrogen Oxygen are formed, leading to energy output.

The fuel cell attempts to harness this electron transfer by spatially separating the reactants, thus allowing the electron exchange over a significantly increased length scale, and this electron exchange can be used as an electric current.
Due to the spatial separation, the original reaction (2.1) can be split into the following two partial reactions [1]

$$H_2 \rightleftharpoons 2\,H^+ + 2\,e^- \tag{2.2}$$

$$\frac{1}{2}\,O_2 + 2\,H^+ + 2\,e^- \rightleftharpoons H_2O. \tag{2.3}$$

As the reaction takes place separately, the electrons are forced to move across an external conductor. The partial reactions take place at the electrodes, i.e. at the anode and cathode. They are separated by an electrolyte, which only conducts protons, i.e., positively charged atoms, but not electrons. Figure 2.3 illustrates the partial reaction of the fuel cell.

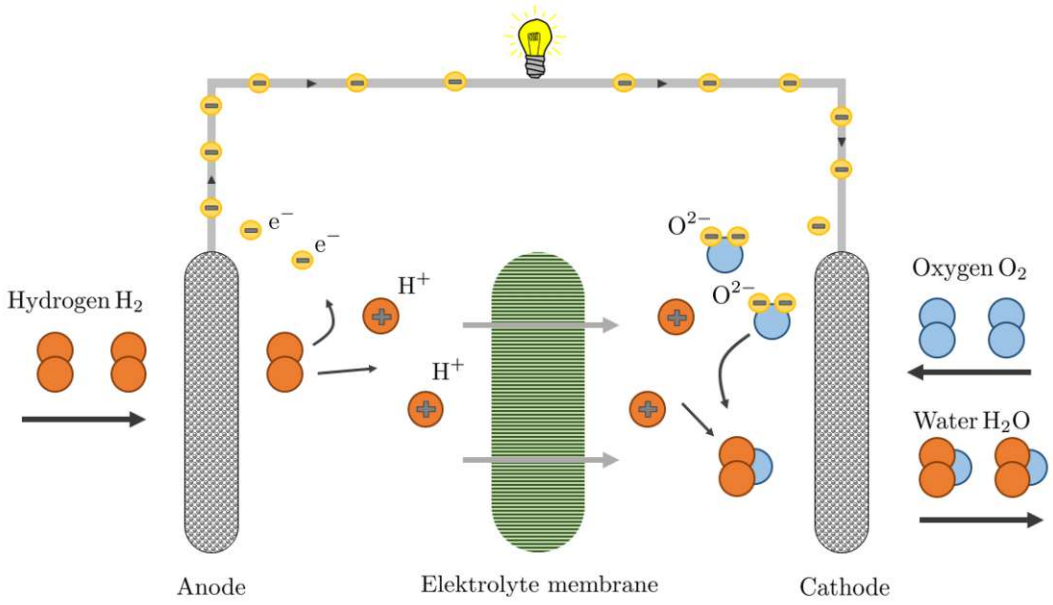

Figure 2.3: Operating principle of a fuel cell [2].

2.1.3 Types of fuel cells

Fuel cells are classified according to the type of electrolyte used. Based on this, one can distinguish between the following five types of fuel cells [1, 22]:

- Polymer electrolyte membrane fuel cell (PEMFC)
- Phosphoric acid fuel cell (PAFC)
- Alkaline fuel cell (AFC)
- Molten carbonate fuel cell (MCFC)
- Solid-oxide fuel cell (SOFC).

All these variants are based on the same electrochemical principle but differ in their operating temperatures, what type of fuel can be used, and their performance characteristics.

	PEMFC	PAFC	AFC	MCFC	SOFC
Electrolyte	Polymer membrane	Phosphoric acid	Potassium hydroxide	Alkali metal carbonates	Ceramic
Operating temperature	80°C	200°C	60-220°C	650°C	600-1000°C
Fuel compatibility	H_2, methanol	H_2	H_2	H_2, CH_4	H_2, CH_4, CO
Applications	Automotive, stat. and portable PG	Stat. PG in container	Space travel	Stat. PG	Stat. and portable PG

Table 2.1: Classification of fuel cells [1]. PG is short for power generation.

Table 2.1 shows the most important distinguishing features of the different fuel cell concepts. Each of these variants has its advantages and disadvantages. Specific consideration must be made for each application for choosing the most suitable variant. For example, low-temperature fuel cells, such as PEMFC or AFC, are more suitable for automotive applications due to their fast start-up behaviour.
In this work, a polymer electrolyte membrane fuel cell model is developed, which is the most suitable variant for the automotive industry.

2.2 PEMFC model

2.2.1 Modelling approaches

There are a lot of different models of polymer electrolyte membrane fuel cells available in the literature. In the following section, the most important differences are shown how these models differ from each other [23].

Spatial dimensions

The first characteristic according to which the models can be categorised is the spatial dimension.

- **0D:** Physical equations with scalar variables describe zero-dimensional models. The spatial change of the system variables cannot be represented, such as the temperature distribution within the fuel cell stack. The description of the voltage

drop with increasing current is in most cases described by a zero-dimensional model, as in [24] for example.

- **1D/2D/3D:** Basically, these models only differ in the number of spatial dimensions that are considered when modelling the physical processes. One possible approach to varying a physical state variable in a spatial dimension is implemented in [25]. This work considers the temperature distribution between the individual cells in the stack in the passage plane. In [26], a two-dimensional model of the Membrane Electrode Assembly (MEA) is used, which considers the variation of temperature, pressure, humidity and oxygen concentration on the surface of the MEA. Three-dimensional models can be used to study various phenomena or the design of components but are not suitable for control engineering applications like typical CFD models. In [27] a complete three-dimensional model of the MEA and the gas distribution channels and considers all significant transport phenomena except phase changes. This model can obtain the three-dimensional distribution of reactant flows, current density, temperature, and water flows.

In this thesis, a model is created which depicts the fundamental relationship between the input variable, the stack current I_{st}, and the output variable, the output voltage of the fuel cell stack V_{st}, as a function of the state variable $\boldsymbol{x}$. Since this relationship is to be mapped in the simplest possible way, a zero-dimensional model is chosen.

Temporal behaviour

Based on the temporal behaviour, a distinction is made between dynamic and static models. In static models, the relationship between the physical quantities is independent of time. The net water flux per proton is statically mapped in the model [28]. Fundamentally, time-dependent phenomena can also be described with quasi-static equations. If a dynamic process can be modelled statically depends on the respective time constant of the process and the relationship to the characteristic ones of the system. For example, according to [6], electrochemical processes reach their steady-state within an order of $\mathrm{O}(10^{-19}\mathrm{sec})$. For comparison, membrane moisture has a time constant of the order $\mathrm{O}(10^{0}\mathrm{sec})$, and thus, the transient effects in electrochemical processes can be neglected and represented by static approaches.
However, most processes are time-dependent and must be modelled dynamically to achieve satisfactory model accuracy. In [29], a static electrochemical model is extended by the effects of mass and heat transfer to predict the transient response of the fuel cell stack during, for example, load steps.

Types of equations

A model of a PEM fuel cell is built up from physical equations. These equations can be divided into three categories: analytical, semi-empirical and empirical equations.
Analytical models, which can also be termed white box models, are based on fundamental physical equations, such as balance equations. Each of these formulas describes a physical phenomenon or process. Another feature of analytic equations is that each variable and parameter has a well-defined meaning. In many cases, the parameters can be derived from the specific properties of the materials used. However, if the material characteristics are not known, they can be determined experimentally. Furthermore, it should be noted that analytical equations are generally valid and not only for the specific case of the PEM fuel cell. A disadvantage of analytical models is that the basic equations are often complex, resulting in a computationally intensive model. The two catalyst layers, the membrane and cathode gas diffuser of a PEM fuel cell, are described in [30] by a fully analytical model to investigate cell voltage limiting factors and species transport in complex networks.
In empirical models or black-box models, the equations are derived from experimentally determined data. In some cases, equations can be derived easily because they are an interpolation curve of the experimental data. These mathematical expressions can often be obtained by simplifying the analytical equations and fitting them to the empirically determined data. This also limits the range of validity of the equations to the content represented by the experiment. In [31] the electrochemical model is built purely from experimentally determined formulas.
Semi-empirical models are a combination of analytical and empirical models and are therefore also called grey-box models. Many phenomena or processes can only be represented inadequately or not at all by analytic equations. In these cases, a mixture of both model types can be used, as in [6], which is used as a modelling guideline for this work. By incorporating the empirical equations, the model thus loses its general validity.

2.2.2 Model assumptions

Based on these considerations, the model used in this thesis aims to represent the fundamental relationships between the stack current I_{st} and the output voltage V_{st} based on the necessary state variables. To keep the scope and complexity of the model manageable, the following assumptions are made for modelling:

- The system boundaries are placed around the stack.
- All gases are assumed to be ideal.

- The temperature of the entire system is uniform and constant.
- No liquid water is taken into account.
- The anode is in dead-end mode. No purge processes are simulated.
- All additionally required inputs are assumed to be known and combined in a parameter vector $\boldsymbol{\theta}$.

The basis for modelling the PEM fuel cell in this work is the work of Pukrushpan [6]. The model in [6] represents a linkage of zero-dimensional container models and it includes the fuel cell stack, the forward and return manifolds and associated auxiliary components such as compressor, humidifier and cooler. Pukrushpan's model is developed from a control engineering point of view, and the system behaviour is mapped with the help of nine states. In particular, the stack model represents the general system behaviour of a PEMFC. In the electrochemical model, an attempt is made to replace some of the empirical equations from [6] with generally valid physical equations from [1] and [22]. The schematic structure of the applied FC model in block diagram form is shown in Figure 2.4. Since the system boundaries of the model are placed around the stack and the auxiliary components are not mapped, the presented model is described with only 5 states in contrast to [6]. The entire model can be decomposed analogously to [6] into the four submodels anode, cathode, membrane and electrochemical model, which are explained in detail in the following.

I_{st} ...	Stackcurrent
V_{st} ...	Stackvoltage
$\xi_{\mathrm{O_2,ca,in}}$ ...	Mass fraction O_2 of the ambient air
$\Lambda_{\mathrm{O_2}}$ ...	Stoichiometric ratio
$\phi_{\mathrm{ca,in}}$ ...	Relative humidity of the ambient air
$p_{\mathrm{ca,in}}$ ...	Cathode input mass flow pressure
T_{st} ...	Stack temperature
$m_{\mathrm{O_2,ca}}$ ...	Mass O_2 cathode
$m_{v,\mathrm{ca}}$...	Mass water vapour cathode
$m_{\mathrm{H_2,an}}$...	Mass H_2 anode
$m_{v,\mathrm{an}}$ ...	Mass vapour anode
λ_{m} ...	Average membrane humidity
$p_{\mathrm{O_2,ca}}$ ...	O_2 partial pressure cathode
$p_{\mathrm{H_2,an}}$ ...	H_2 partial pressure anode
ϕ_{ca} ...	Relative humidity in the cathode
ϕ_{an} ...	Relative humidity in the anode

p_{ca} ... Pressure cathode
$W_{\text{v,membr}}$ ... Membrane water vapour mass flow

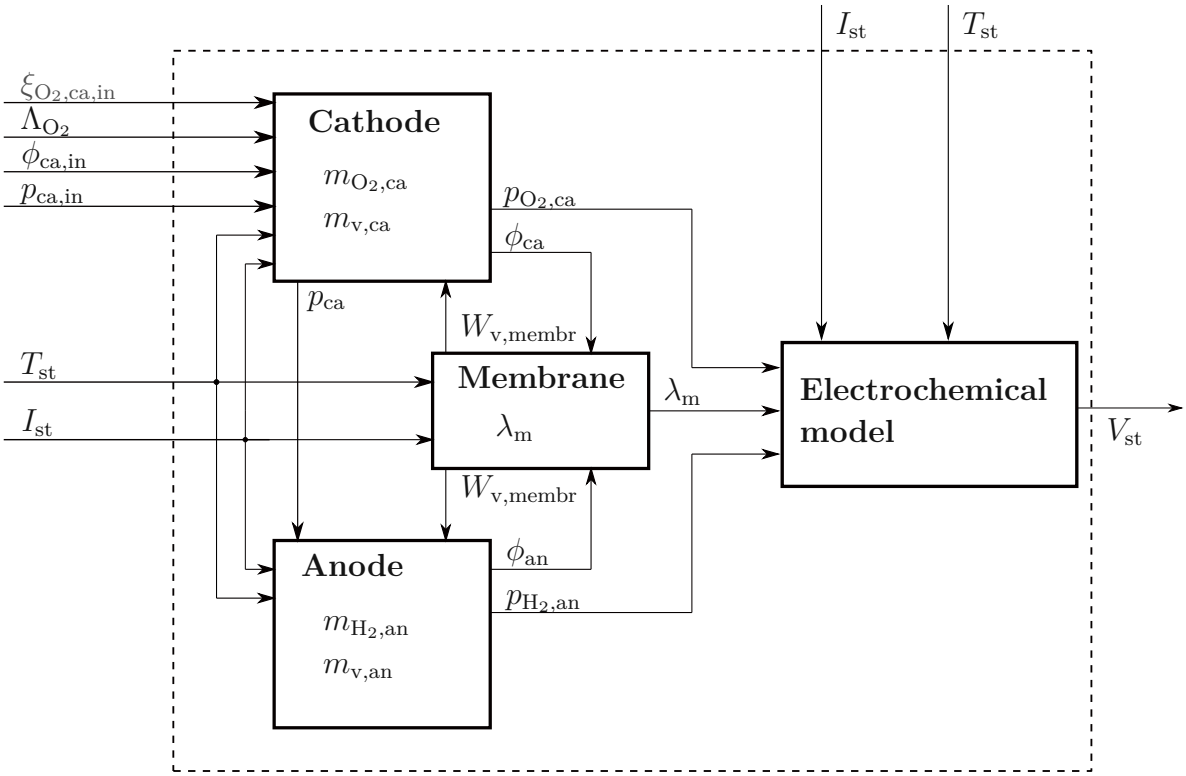

Figure 2.4: Block diagram of the PEMFC model

2.2.3 Cathode model

The cathode model maps the mass flows in the cathode and relates the mass flow's transient effects to the static electrochemical model. The behaviour of the state variables in the cathode is determined by the mass balance and the thermodynamic properties of the gases, as in the zero-dimensional models in [6] and [32]. Balancing the input and output mass flow rates results in the following system equations for the cathode

$$\frac{dm_{\mathrm{O_2,ca}}}{dt} = W_{\mathrm{O_2,ca,in}} - W_{\mathrm{O_2,ca,out}} - W_{\mathrm{O_2,ca,reacted}} \tag{2.4}$$

$$\frac{dm_{\mathrm{N_2,ca}}}{dt} = W_{\mathrm{N_2,ca,in}} - W_{\mathrm{N_2,ca,out}} \tag{2.5}$$

$$\frac{dm_{\mathrm{v,ca}}}{dt} = W_{\mathrm{v,ca,in}} - W_{\mathrm{v,ca,out}} + W_{\mathrm{v,ca,gen}} + W_{\mathrm{v,membr}} \tag{2.6}$$

where $m_{\mathrm{O_2,ca}}$ (kg) is the oxygen mass in the cathode, $W_{\mathrm{O_2,ca,in}}$ (kg/s) the input mass flow of oxygen into the cathode, $W_{\mathrm{O_2,ca,out}}$ (kg/s) the output mass flow of oxygen from the cathode, $m_{\mathrm{N_2,ca}}$ (kg) is the nitrogen mass in the cathode, $W_{\mathrm{N_2,ca,in}}$ (kg/s) the input mass flow of nitrogen into the cathode, $W_{\mathrm{N_2,ca,out}}$ (kg/s) the output mass flow of nitrogen from the cathode, $W_{\mathrm{O_2,reacted}}$ (kg/s) the mass flow of reacted oxygen, $m_{\mathrm{v,ca}}$ (kg) the water vapor mass in the cathode, $W_{\mathrm{v,ca,in}}$ (kg/s) the input mass flow of water vapor into the cathode, $W_{\mathrm{v,ca,out}}$ (kg/s) the output mass flow of water vapor from the cathode, $W_{\mathrm{v,ca,gen}}$ (kg/s) the water vapour mass flow generated by the reaction and $W_{\mathrm{v,membr}}$ (kg/s) the water vapour mass flow across the membrane.
The partial pressures of oxygen $p_{\mathrm{O_2,ca}}$, the partial pressures of nitrogen $p_{\mathrm{N_2,ca}}$ and water vapour $p_{\mathrm{v,ca}}$ in the cathode are obtained from the ideal gas equation

$$p_{\mathrm{O_2,ca}} = \frac{m_{\mathrm{O_2,ca}} R\, T_{\mathrm{st}}}{V_{\mathrm{ca}} M_{\mathrm{O_2}}} \tag{2.7}$$

$$p_{\mathrm{N_2,ca}} = \frac{m_{\mathrm{N_2,ca}} R\, T_{\mathrm{st}}}{V_{\mathrm{ca}} M_{\mathrm{N_2}}} \tag{2.8}$$

$$p_{\mathrm{v,ca}} = \frac{m_{\mathrm{v,ca}} R\, T_{\mathrm{st}}}{V_{\mathrm{ca}} M_{\mathrm{v}}} \tag{2.9}$$

where T_{st} (K) is the stack temperature, which is constant for the entire system, R (J/ (mol K)) the universal gas constant, V_{ca} (m^3) the volume of the cathode, $M_{\mathrm{O_2}}$ (kg/mol) the molar mass of oxygen, $M_{\mathrm{N_2}}$ (kg/mol) the molar mass of nitrogen and M_{v} (kg/mol) the molar mass of water vapour.
The total pressure of dry air in the cathode $p_{\mathrm{a,ca}}$ (Pa) and humid air p_{ca} (Pa) are composed of the individual partial pressures

$$p_{\mathrm{a,ca}} = p_{\mathrm{O_2,ca}} + p_{\mathrm{N_2,ca}} \tag{2.10}$$

$$p_{\mathrm{ca}} = p_{\mathrm{a,ca}} + p_{\mathrm{v,ca}}. \tag{2.11}$$

One output of the cathode submodel is the relative humidity ϕ_{ca} which is defined as follows

$$\phi_{\text{ca}} = \frac{p_{\text{v,ca}}}{p_{\text{sat}}(T_{\text{st}})} \tag{2.12}$$

where p_{sat} (Pa) is the saturation vapour pressure at stack temperature T_{st}.

On the cathode side, the fuel cell is supplied with ambient air. This mass flow is usually provided by a compressor, cooled and brought to the desired humidity. In this simplified representation of the fuel cell, it is assumed that this mass flow of humid air is given as an input variable at any time and that the mass flow is adjusted accordingly depending on the operating point or the stack current I_{st}. To calculate this cathode input mass flow, the stoichiometric coefficient Λ_{O_2} is required, which defines the mass flow ratio between the inflowing and consumed oxygen

$$\Lambda_{\text{O}_2} = \frac{W_{\text{O}_2,ca,in}}{W_{\text{O}_2,\text{ca,reacted}}}. \tag{2.13}$$

The input mass flow $W_{\text{ca,in}}$ is set as a function of the input current I_{st} and the parameter Λ_{O_2}. The mass flow of reacted oxygen in the cathode $W_{\text{O}_2,\text{ca,reacted}}$ in equation (2.15) can be determined using Faraday's law

$$W_{\text{ca,in}} = \frac{\Lambda_{\text{O}_2} \cdot (1 + \omega_{\text{ca,in}})}{\psi_{\text{O}_2,\text{ca,in}}} \cdot W_{\text{O}_2,\text{ca,reacted}} \tag{2.14}$$

$$W_{\text{O}_2,\text{reacted}} = M_{\text{O}_2} \cdot \frac{n_{\text{cells}} I_{\text{st}}}{4F} \tag{2.15}$$

$$\psi_{\text{O}_2,\text{ca,in}} = \frac{\xi_{\text{O}_2,\text{ca,in}} \cdot M_{\text{O}_2}}{\xi_{\text{O}_2,\text{ca,in}} \cdot M_{\text{O}_2} + (1 - \xi_{\text{O}_2,\text{ca,in}}) \cdot M_{\text{N}_2}} \tag{2.16}$$

$$\omega_{\text{ca,in}} = \frac{M_{\text{v}}}{M_{\text{a,ca,in}}} \frac{p_{\text{v,ca,in}}}{p_{\text{a,ca,in}}} \tag{2.17}$$

$$M_{\text{a,ca,in}} = \xi_{\text{O}_2,\text{ca,in}} \cdot M_{\text{O}_2} + (1 - \xi_{\text{O}_2,\text{ca,in}}) \cdot M_{\text{N}_2}. \tag{2.18}$$

In equations (2.14) to (2.18), is $\omega_{\text{ca,in}}$ the humidity ratio, $\psi_{\text{O}_2,\text{ca,in}}$ the oxygen mass fraction of the input mass flow, n_{cells} the number of cells, F (C/mol) Faraday constant, $\xi_{\text{O}_2,\text{ca,in}}$ the oxygen mole fraction of the inlet air (i.e. the ambient air), M_{v} (kg/mol) the molar mass of water vapour, $M_{\text{a,ca,in}}$ (kg/mol) the olar mass of air, $p_{\text{v,ca,in}}$ (Pa) the water vapour partial pressure of the inlet air and $p_{\text{a,ca,in}}$ (Pa) the partial pressure of dry incoming air.
The incoming mass flow of humid air can be split into the specific mass flows needed for the state equations (2.4) and (2.6)

$$W_{\mathrm{a,ca,in}} = \frac{1}{1+\omega_{\mathrm{ca,in}}} W_{\mathrm{ca,in}} \tag{2.19}$$

$$W_{\mathrm{v,ca,in}} = W_{\mathrm{ca,in}} - W_{\mathrm{a,ca,in}} \tag{2.20}$$

$$W_{\mathrm{O_2,ca,in}} = \psi_{\mathrm{O_2,ca,in}} W_{\mathrm{a,ca,in}} \tag{2.21}$$

$$W_{\mathrm{N_2,ca,in}} = (1-\psi_{\mathrm{O_2,ca,in}})\, W_{\mathrm{a,ca,in}} \tag{2.22}$$

$$\psi_{\mathrm{O_2,ca,in}} = \frac{\xi_{\mathrm{O_2,ca,in}} \cdot M_{\mathrm{O_2}}}{\xi_{\mathrm{O_2,ca,in}} \cdot M_{\mathrm{O_2}} + (1-\xi_{\mathrm{O_2,ca,in}}) \cdot M_{\mathrm{N_2}}} \tag{2.23}$$

$$p_{\mathrm{v,ca,in}} = \phi_{\mathrm{ca,in}} \cdot p_{\mathrm{sat}}(T_{\mathrm{st}}) \tag{2.24}$$

$$p_{\mathrm{a,ca,in}} = p_{\mathrm{ca,in}} - p_{\mathrm{v,ca,in}} \tag{2.25}$$

where $\phi_{\mathrm{ca,in}}$ is the relative humidity of the incoming ambient air, $p_{\mathrm{v,ca,in}}$ (Pa) the water vapour partial pressure of the cathode input mass flow, $p_{\mathrm{a,ca,in}}$ (Pa) dry air partial pressure of the cathode input mass flow and $p_{\mathrm{ca,in}}$ (Pa) the total pressure of the cathode input mass flow.

The output mass flow $W_{\mathrm{ca,out}}$ (kg/s) is assumed to be proportional to the pressure difference between the cathode and the environment. Another assumption is that there is ambient pressure at the exit of the cathode. As in [6], a linear orifice equation is used to calculate the output mass flow $W_{\mathrm{ca,out}}$ as

$$W_{\mathrm{ca,out}} = k_{\mathrm{ca,out}} \left(p_{\mathrm{ca}} - p_{\mathrm{atm}}\right). \tag{2.26}$$

With the state variables,the partial pressures and the specific properties of the gases, the output mass flow is divided into the specific mass flows for state equations (2.4) and (2.6)

$$\xi_{\mathrm{O_2,ca}} = \frac{p_{\mathrm{O_2,ca}}}{p_{\mathrm{a,ca}}} \tag{2.27}$$

$$\psi_{\mathrm{O_2,ca}} = \frac{\xi_{\mathrm{O_2,ca}} \cdot M_{\mathrm{O_2}}}{\xi_{\mathrm{O_2,ca}} \cdot M_{\mathrm{O_2}} + (1-\xi_{\mathrm{O_2,ca}}) \cdot M_{\mathrm{N_2}}} \tag{2.28}$$

$$M_{\mathrm{a,ca}} = \xi_{\mathrm{O_2,ca}} \cdot M_{\mathrm{O_2}} + (1-\xi_{\mathrm{O_2,ca}}) \cdot M_{\mathrm{N_2}} \tag{2.29}$$

$$\omega_{\mathrm{ca,out}} = \frac{M_{\mathrm{v}}}{M_{\mathrm{a,ca}}} \frac{p_{\mathrm{v,ca}}}{p_{\mathrm{a,ca}}} \tag{2.30}$$

$$W_{\mathrm{a,ca,out}} = \frac{1}{1+\omega_{\mathrm{ca,out}}} W_{\mathrm{ca,out}} \tag{2.31}$$

$$W_{\mathrm{v,ca,out}} = W_{\mathrm{ca,out}} - W_{\mathrm{a,ca,out}} \tag{2.32}$$
$$W_{\mathrm{O_2,ca,out}} = \psi_{\mathrm{O_2,ca}} W_{\mathrm{a,ca,out}} \tag{2.33}$$
$$W_{\mathrm{N_2,ca,out}} = (1 - \psi_{\mathrm{O_2,ca}})\, W_{\mathrm{a,ca,out}} \tag{2.34}$$

where $\xi_{\mathrm{O_2,ca}}$ is the oxygen mole fraction in the cathode, $\psi_{\mathrm{O_2,ca}}$ the oxygen mass fraction in the cathode, $M_{\mathrm{a,ca}}$ (kg/mol) the dry air molar mass in the cathode, $\omega_{\mathrm{ca,out}}$ humidity ration of the cathode output mass flow and $W_{\mathrm{a,ca,out}}$ (kg/s) the dry air cathode output mass flow.

Faraday's law describes the relationship between electric charge and the turnover of substances in electrochemical reactions. From this basic law, it can be derived that the current density is proportional to the transferred charges and the consumption of the reactants [22]. The mass flows of reacted oxygen in the cathode $W_{\mathrm{O_2,ca,reacted}}$ and the water vapour formed in the process $W_{\mathrm{v,ca,gen}}$ are calculated as a function of the current I_{st} as follows

$$W_{\mathrm{O_2,reacted}} = M_{\mathrm{O_2}} \cdot \frac{n_{\mathrm{cells}} I_{\mathrm{st}}}{4F} \tag{2.35}$$
$$W_{\mathrm{v,ca,gen}} = M_{\mathrm{v}} \cdot \frac{n_{\mathrm{cells}} I_{\mathrm{st}}}{2F} \tag{2.36}$$

where n_{cells} is the number of cells placed in series.

2.2.4 Anode model

The structure of the anode submodel is the same as for the cathode. The dynamics of the model are determined by the mass balance of the specific mass flows. It is assumed, as in the work of Pukrushpan [6], that the anode is operated in dead-end mode, and the hydrogen and water vapour can only escape from the fuel cell through a cyclically opening valve, the so-called purge valve. This purge process drains the accumulated liquid water and nitrogen from the anode during operation, causing the hydrogen concentration to rise again. In this simplified model and the associated simulation, only the scenarios in which the purge valve is closed are dealt with.
The dynamic behaviour of the submodel is determined by the hydrogen mass $m_{\mathrm{H_2,an}}$ (kg) and water vapour mass $m_{\mathrm{v,an}}$ (kg). As in the cathode, these states are defined by balancing the input and output flows as follows

$$\frac{dm_{\mathrm{H_2,an}}}{dt} = W_{\mathrm{H_2,an,in}} - W_{\mathrm{H_2,an,out}} - W_{\mathrm{H_2,an,reacted}} \tag{2.37}$$

$$\frac{m_{\mathrm{v,an}}}{dt} = -W_{\mathrm{v,membr}} - W_{\mathrm{v,an,out}} \tag{2.38}$$

where $W_{\mathrm{H_2,an,in}}$ (kg/s) is the input mass flow of pure dry hydrogen, $W_{\mathrm{H_2,an,reacted}}$ (kg/s) is the mass flow of oxidized hydrogen in the anode. $W_{\mathrm{H_2,an,out}}$ (kg/s) and $W_{\mathrm{v,an,out}}$ (kg/s) are the output mass flows of hydrogen and water vapour, respectively, which are set to zero in this simplified representation of the fuel cell. This means, that the amount of hydrogen that is currently being consumed is fed into the anode.
Using the thermal equation of state for ideal gases, the partial pressures of hydrogen $p_{\mathrm{H_2,an}}$ (Pa) and water vapour $p_{\mathrm{v,an}}$ (Pa) and the resulting total pressure in the anode p_{an} (Pa) can be calculated

$$p_{\mathrm{H_2,an}} = \frac{m_{\mathrm{H_2,an}} R T_{\mathrm{st}}}{V_{\mathrm{an}} M_{\mathrm{H_2}}} \tag{2.39}$$

$$p_{\mathrm{v,an}} = \frac{m_{\mathrm{v,an}} R T_{\mathrm{st}}}{V_{\mathrm{an}} M_{\mathrm{v}}} \tag{2.40}$$

$$p_{\mathrm{an}} = p_{\mathrm{H_2,an}} + p_{\mathrm{v,an}} \tag{2.41}$$

where V_{an} (m^3) is the volume of the anode and $M_{\mathrm{H_2}}$ (kg/mol) is the molar mass of hydrogen. Another assumption to simplify the model is that the anode is supplied directly with pure dry hydrogen from a pressurised bottle. This mass flow is adjusted via a proportional controller so that the pressure difference between anode and cathode is minimised. The anode input mass flow $W_{\mathrm{an,in}}$ which represents a pure hydrogen mass flow $W_{\mathrm{H_2,an,in}}$ results as follows

$$W_{\mathrm{an,in}} = W_{\mathrm{H_2,an,in}} = k_{\mathrm{an,in}} \cdot (p_{\mathrm{an}} - p_{\mathrm{ca}}) \tag{2.42}$$

where $k_{\mathrm{an,in}}$ is the controller gain.
The consumed mass flow of hydrogen can be derived and calculated in the same way as the two equations (2.35) and (2.36). Using Faraday's law, the mass flow of hydrogen $W_{\mathrm{H_2,reacted}}$ consumed in the electrochemical reaction can be calculated as follows

$$W_{\mathrm{H_2,reacted}} = M_{\mathrm{H_2}} \frac{n_{\mathrm{cells}} I}{2F}. \tag{2.43}$$

2.2.5 Membrane model

The zero-dimensional submodel of the membrane represents the average water content of the membrane. As with the cathode and anode model, no spatial change in the state variable, the mean membrane humidity λ_m, is taken into account here.
The material of the membrane was assumed to be Nafion 117 as in [6]. Nafion is a material that can absorb a considerable amount of water due to its pore structure. According to [1], the volume can increase by 22% due to water absorption. Since the conductivity of the membrane correlates strongly with the water content, the water content must be determined in order to calculate the conductivity.

For the membrane model the normalised current density $i\,(\mathrm{A/cm^2})$ is used, which is defined as

$$i = \frac{I_{st}}{A_{fc}} \tag{2.44}$$

where $A_{fc}\,(\mathrm{cm^2})$ is the active area of the fuel cell.
The humidity conditions are evaluated using the water activities $a_{v,ca}$ of the cathode and $a_{v,an}$ of the anode

$$a_{v,an} = \frac{p_{v,an}}{p_{sat}(T_{st})} \tag{2.45}$$

$$a_{v,ca} = \frac{p_{v,ca}}{p_{sat}(T_{st})}. \tag{2.46}$$

Since no spatially varying membrane humidity is considered, the mean of the water activities a_m of cathode and anode is used to calculate the mean membrane humidity based on [6] and formula

$$a_m = \frac{a_{v,an} + a_{v,ca}}{2}. \tag{2.47}$$

Basically, the water content of the membrane λ_m is defined as the ratio of water molecules to charged ($SO_3{}^-H^+$) sites [1]. λ_m can take values from zero, for completely dehydrated Nafion, to 22, completely saturated membrane. When calculating the mean membrane humidity, a distinction is made in [1] between the unsaturated ($a_m <= 1$) and the saturated areas ($a_m > 1$). For this model, however, only the first range is relevant, as no liquid water is considered. The average membrane humidity can be determined with the following empirical equation from [1]

$$\lambda_m = 0.043 + 17.81 a_m - 39.85 a_m^2 + 36 a_m^3. \tag{2.48}$$

To be able to reproduce the transient rewetting of the membrane during current steps in the model, a PT1 element with a time constant $\tau = 2$ seconds is connected downstream as in [9]

$$G_{\mathrm{PT1}}(s) = \frac{K_{\mathrm{PT1}}}{1 + \tau \cdot s} \tag{2.49}$$

where K_{PT1} is the proportional part, which is set to 1. These effects during input steps are also called over- or undershoot effects. One explanation for this is that water is produced during the steps, but needs some time to diffuse into the membrane.
The mass flows of water vapour that pass between the anode and cathode through the membrane are determined by two effects. One phenomenon that triggers a water vapour mass flow is the electroosmotic drag. When protons migrate through the porous structure of the Nafion membrane, they drag several water molecules with them. This effect is quantified by the electroosmotic drag coefficient n_{d}, which describes how many water molecules are dragged along by the movement of a proton. The calculation of this coefficient is done as in [6] with the empirical formula from [33] in dependence of the mean membrane humidity

$$n_{\mathrm{d}} = 0.0029\lambda_{\mathrm{m}}^2 + 0.05\lambda_{\mathrm{m}} - 3.4 \cdot 10^{-19}. \tag{2.50}$$

The molar flux of water vapour through the membrane due to the electro-osmotic resistance $N_{\mathrm{v,osmotic}}$ $(\mathrm{mol}/\,(\mathrm{s\,cm^2}))$ can be calculated as follows [1]

$$N_{\mathrm{v,osmotic}} = n_{\mathrm{d}} \frac{i}{F}. \tag{2.51}$$

Due to the electro-osmotic drag, water vapour migrates from the anode to the cathode. In addition, water vapour is formed in the cathode by the electrochemical reaction. The resulting differences in the concentration of water vapour between the anode and the cathode cause water to diffuse back again. This phenomenon is also called back diffusion. The rate of water diffusion $N_{\mathrm{v,diff}}$ $(\mathrm{mol}/\,(\mathrm{s\,cm^2}))$ is [22]

$$N_{\mathrm{v,diff}} = D_{\mathrm{w}} \frac{dc_{\mathrm{v}}}{dz} = D_{\mathrm{w}} \frac{(c_{\mathrm{v,ca}} - c_{\mathrm{v,an}})}{t_{\mathrm{m}}} \tag{2.52}$$

where D_{w} is the diffusion coefficient of water in the membrane, $c_{v,ca}$ and $c_{\mathrm{v,an}}$ the water concentration in the cathode respectively anode and t_{m} (cm) the membrane thickness. The diffusion coefficient D_{w} is calculated as in [33] as a function of the mean membrane humidity

$$D_{\mathrm{w}} = D_{\lambda} \exp\left(2416\left(\frac{1}{303} - \frac{1}{T_{\mathrm{st}}}\right)\right) \tag{2.53}$$

$$D_{\lambda} = \begin{cases} 10^{-6} & ,\lambda_{\mathrm{m}} < 2 \\ 10^{-6}\left(1 + 2\left(\lambda_{\mathrm{m}} - 2\right)\right) & ,2 \leq \lambda_{\mathrm{m}} \leq 3 \\ 10^{-6}\left(3 - 1.67\left(\lambda_{\mathrm{m}} - 3\right)\right) & ,3 \leq \lambda_{\mathrm{m}} < 4.5 \\ 1.25 \cdot 10^{-6} & ,\lambda_{\mathrm{m}} \geq 4.5. \end{cases}$$

The water concentration in the membrane for the cathode $c_{\mathrm{v,ca}}$ and for the anode $c_{\mathrm{v,an}}$ is calculated based on [22]

$$c_{\mathrm{v,an}} = \frac{\rho_{\mathrm{m,dry}}}{M_{\mathrm{m,dry}}} \lambda_{\mathrm{an}} \tag{2.54}$$

$$c_{\mathrm{v,ca}} = \frac{\rho_{\mathrm{m,dry}}}{M_{\mathrm{m,dry}}} \lambda_{\mathrm{ca}} \tag{2.55}$$

where $\rho_{\mathrm{m,dry}}\,(\mathrm{kg/cm^3})$ is the density of the dry membrane, $M_{\mathrm{m,dry}}\,(\mathrm{kg/mol})$ is the dry equivalent weight of the membrane. λ_{ca} and λ_{an} are the membrane humidities, with the difference that they are not calculated with the mean water activity a_{m} as in equation (2.48), but with the respective water activities of the cathode a_{ca} and anode a_{an}.

The difference between the two molar fluxes yields the absolute molar flux across the membrane $N_{\mathrm{v,membr}}$. This is further converted into a mass flow for the state equations (2.6) and (2.38)

$$N_{\mathrm{v,membr}} = n_{\mathrm{d}} \frac{i}{F} - D_{\mathrm{w}} \frac{(c_{\mathrm{v,ca}} - c_{\mathrm{v,an}})}{t_{\mathrm{m}}} \tag{2.56}$$

$$W_{\mathrm{v,membr}} = N_{\mathrm{v,membr}} \cdot M_{\mathrm{v}} \cdot A_{\mathrm{fc}} \cdot n_{\mathrm{cells}} \tag{2.57}$$

where $A_{\mathrm{fc}}\,(\mathrm{cm^2})$ is the active area of the fuel cell.

2.2.6 Electrochemical model

In the electrochemical model, the output voltage of the fuel cell is calculated from the states and the resulting partial pressure. The zero-dimensional sub-model is based on the polarisation curve, in which the theoretical open-circuit voltage and the three loss voltages (activation loss, ohmic voltage drop and concentration loss) result in the actual output voltage.

As mentioned in Section 2.1.2, the fuel cell converts chemically bonded energy into electrical energy. The following overall reaction takes place in a PEM fuel cell

$$\mathrm{H_2} + \frac{1}{2}\,\mathrm{O_2} \longrightarrow \mathrm{H_2O}. \tag{2.58}$$

In electrochemical systems, such as the fuel cell, the Gibbs free energy indicates the maximum amount of energy that can perform electrical work. At constant temperature, the Gibbs energy can be expressed in molar form $\Delta\hat{g}\,(\mathrm{J/mol})$ as follows [1]

$$\Delta\hat{g} = \Delta\hat{h} + T\Delta\hat{s} \tag{2.59}$$

where $\Delta\hat{h}\,(\mathrm{J/mol})$ is the difference in enthalpy between reactants and products, $\Delta\hat{s}\,(\mathrm{J/\,(mol\,K)})$ is the difference in entropy between reactants and products and $T\,(\mathrm{K})$ the temperature. The electrical work $W_{\mathrm{el}}\,(\mathrm{J/mol})$ performed by the two electrons per hydrogen molecule in the external electrical conductor is defined as [22]

$$W_{\mathrm{el}} = 2FE \tag{2.60}$$

where $E\,(\mathrm{V})$ is the potential. This electric work is equal to the negative of the Gibbs free energy difference for a process with constant pressure and temperature [1]

$$\Delta\hat{g} = -2FE. \tag{2.61}$$

From Equation (2.61), the reversible voltage $E_0\,(\mathrm{V})$ of the fuel cell given standard conditions (25 °C unit temperature and 1 atm unit pressure) is obtained for a hydrogen-oxygen fuel cell [1]

$$E_0 = -\frac{\Delta\hat{g}^0}{2F} = 1.23V \tag{2.62}$$

where $\Delta\hat{g}^0\,(\mathrm{J/mol})$ is the standard-state free-energy change. If, as in [1], the influences of temperature, pressure and concentrations on the Gibbs energy are also taken into account, the following description of the reversible fuel cell voltage is obtained

$$E = E^0 + \frac{\Delta\hat{s}}{nF}\,(T_{\mathrm{st}} - T_0) - \frac{RT_{\mathrm{st}}}{2F}\ln\frac{\prod a_{\mathrm{products}}^{v_i}}{\prod a_{\mathrm{reactants}}^{v_i}} \tag{2.63}$$

where $T_0\,(\mathrm{K})$ is the standard-state temperature (25°C), a_i the activities of the gases, which can be replaced by the partial pressures in atm and v_i are the corresponding

stoichiometric coefficients. The entropy change can be assumed to be constant because the variation of the specific heat at the assumed stack temperature is minimal. By inserting the entropy at standard state condition and further extending the equation, the following formulation is obtained from [34] for the reversible cell voltage [6] as

$$E = 1.229 - 0.85 \cdot 10^{-3} \cdot (T_{\text{st}} - 298.15) + 4.3085 \cdot 10^{-5} \cdot T_{\text{st}} \left(ln(p_{\text{H}_2,\text{an}}) + \frac{1}{2} ln(p_{\text{O}_2,\text{ca}}) \right) \tag{2.64}$$

where the partial pressure $p_{\text{O}_2,ca}$ and $p_{\text{H}_2,an}$ are in atm.

However in practice the actual cell voltage deviates from the theoretical potential and is typically smaller. The following factors can cause such voltage losses in a fuel cell [22]:

- kinetics of the electrochemical reactions
- internal electrical and ionic resistance
- difficulties in getting the reactants to reaction site
- internal (stray) currents
- crossover of reactants

To keep the model's scope manageable, only the following three significant losses are considered in this thesis.

Activation loss

The activation loss is caused by breaking and reforming of chemical bonds. This energy cannot be used and is therefore perceived lost. These losses occur at the cathode as well as at the anode, but the oxygen reduction requires a higher overvoltage than the hydrogen oxidation. In [1], the activation loss V_{act} (V) is calculated using a simplified form of the Butler-Volmer equation

$$V_{\text{act}} = \frac{RT_{\text{st}}}{\alpha 2F} \ln \left(\frac{i}{i_0} \right) \tag{2.65}$$

where i_0 (A/cm^2) is the exchange current density, which is constant and a measure of the reactivity at the electrode surfaces and α is the transfer coefficient.

Ohmic loss

The transport of charges causes a further voltage drop in the fuel cell. A distinction is made between ionic and electronic charge transport, whereby the ionic one is the dominant resistance [1]. Therefore, only the ionic charge transport is considered in the simplified model. The voltage drop $V_{\text{ohm}}\,(\text{V})$ caused by the charge transport is calculated similarly to Ohm's law [1]

$$V_{\text{ohm}} = i\frac{t_{\text{m}}}{\sigma} \tag{2.66}$$

where $t_{\text{m}}\,(\text{cm})$ is the membrane thickness and $\sigma\,(\Omega/\text{m})$ the proton conductivity of the membrane. The ionic conductivity of the membrane depends on the water content and the temperature. The empirical formulae for determining the conductivity of the Nafion membrane are taken from [1], which are also used in [6].

$$\sigma = \sigma_{303K}(\lambda_{\text{m}}) \cdot \exp\left[1268\left(\frac{1}{303} - \frac{1}{T_{\text{st}}}\right)\right] \tag{2.67}$$

$$\sigma_{303\text{K}}(\lambda_{\text{m}}) = 0.005193\lambda_{\text{m}} - 0.00326. \tag{2.68}$$

Concentration loss

The third loss considered in this model is the concentration loss $V_{\text{conc}}\,(\text{V})$. This effect occurs when the reactants are rapidly consumed, such as at high current densities, resulting in concentration gradients. The estimation of these voltage drops is analogous to [6] based on the following empirical formula [35]

$$V_{\text{conc}} = i \cdot \left(a\frac{i}{i_{\text{lim}}}\right)^2 \tag{2.69}$$

where $i_{\text{lim}}\,(\text{A/cm}^2)$ is the limiting current density and a is a constant, which is determined empirically and depending on the partial pressures and the temperature. The calculation of the constant a is [6]

$$a = \begin{cases} (7.16 \cdot 10^{-4} T_{\text{st}} - 0.622)\left(\frac{p_{\text{O2,ca}}}{0.1173} + p_{\text{sat}}\right) & \\ \quad + (-1.45 \cdot 10^{-3} T_{\text{st}} + 1.68) & \text{for } \left(\frac{p_{\text{O2,ca}}}{0.1173} + p_{\text{sat}}\right) < 2\,\text{atm} \\ (8.66 \cdot 10^{-5} T_{\text{st}} - 0.068)\left(\frac{p_{\text{O2,ca}}}{0.1173} + p_{\text{sat}}\right) & \\ \quad + (-1.6 \cdot 10^{-4} T_{\text{st}} + 0.54) & \text{for } \left(\frac{p_{\text{O2,ca}}}{0.1173} + p_{\text{sat}}\right) \geq 2\,\text{atm}. \end{cases}$$

Based on the reversible cell voltage of Equation (2.64) and the three loss voltages from Equations (2.65), (2.66) and (2.69), the actual cell voltage V_{cell} is calculated as

$$V_{\text{cell}} = E - V_{\text{act}} - V_{\text{ohm}} - V_{\text{conc}}. \tag{2.70}$$

The total voltage of the fuel cell stack V_{st}, which again represents the main output of the fuel cell model, results from the multiplication of the n_{cells} fuel cells connected in series, given by

$$V_{\text{st}} = n_{\text{cells}} V_{\text{cell}}. \tag{2.71}$$

Since the mass of nitrogen in the cathode turns out to be unobservable in this model configuration, it is represented via a static relation. Criteria for the observability of state-space models are discussed in more detail in Section 3.1.3. If one sets the change in nitrogen mass in Equation (2.5) to zero and uses the Equations (2.22) and (2.34) accordingly, the following expression for the nitrogen partial pressure in the cathode can be derived

$$p_{\text{N}_2,\text{ca}} = \frac{W_{\text{N}_2,\text{ca,in}}}{k_{\text{ca,out}}\left(1 - \psi_{\text{O}_2,ca}\right)} - p_{\text{O}_2,\text{ca}} - p_{\text{v,ca}} - p_{\text{atm}} \tag{2.72}$$

where $k_{\text{ca}_\text{o}\text{ut}}$ a constant value coefficient is.
For the derivation and implementation of the state observer in Chapter 3, the model of the PEM fuel cell is summarised in the following non-linear state space representation

$$\dot{\boldsymbol{x}} = \boldsymbol{f}\left(\boldsymbol{x}, \boldsymbol{u}, \boldsymbol{\Theta}\right) \tag{2.73}$$

$$\boldsymbol{x} = \begin{bmatrix} m_{\text{O}_2,\text{ca}} & m_{\text{v,ca}} & m_{\text{H}_2,\text{an}} & m_{\text{v,an}} & \lambda_{\text{m}} \end{bmatrix}^T \tag{2.74}$$

$$\boldsymbol{\theta} = \begin{bmatrix} \xi_{\text{O}_2,\text{ca,in}} & \Lambda_{\text{O}_2} & \phi_{\text{ca,in}} & p_{\text{ca,in}} & T_{\text{st}} \end{bmatrix}^T$$

$$u = I_{\text{st}}$$

$$y = V_{\text{st}}$$

2.3 Simulation of the PEMFC system

Since this model of the PEM fuel cell is used to validate the observer concept, the model is not parametrised for a specific fuel cell stack. It is intended to represent the fundamental relationship between the states, input and output. The characteristic system

parameters used for modelling are taken from various sources. The parameters are used for the system simulation, shown in Table 2.3.

Parameter	Unit	Value	Reference
$p_{\mathrm{ca,in}}$	$1.5 \cdot 10^5$	Pa	
$p_{\mathrm{sat}}(T_{\mathrm{st}})$	$4.6693 \cdot 10^4$	Pa	
p_{atm}	101325	Pa	
$\xi_{\mathrm{O_2,ca,in}}$	0.21		
$\phi_{\mathrm{ca,in}}$	0.4		
F	96485.332	F	
R	8.311463	J/(mol K)	
$\Lambda_{\mathrm{O_2}}$	2		
$M_{\mathrm{O_2}}$	$31.9988 \cdot 10^{-3}$	kg/mol	
$M_{\mathrm{N_2}}$	$28.0134 \cdot 10^{-3}$	kg/mol	
$M_{\mathrm{H_2}}$	$2.01588 \cdot 10^{-3}$	kg/mol	
M_{v}	$18.01528 \cdot 10^{-3}$	kg/mol	
$M_{\mathrm{m,dry}}$	1.1	kg/mol	[6]
V_{an}	0.005	m^3	[6]
V_{ca}	0.01	m^3	[6]
T_{st}	353.15	K	
n_{cells}	381		[6]
A_{fc}	280	cm^2	[6]
t_{m}	0.01275	cm	[6]
$k_{\mathrm{ca,out}}$	$1.5239 \cdot 10^{-6}$		
$\rho_{\mathrm{m,dry}}$	$2 \cdot 10^{-3}$		
i_0	10^{-4}	$\mathrm{A/cm}^2$	[1]
α	0.5		[1]

Table 2.3: Simulation parameters for the FC model

The simulation of start-up processes is not included in the scope of this work. The initial states of the system simulation are chosen such that the simulation at time $t = 0\,\mathrm{s}$ represents typical operation and not a "cold start" at ambient conditions. The following initial states are chosen for the simulation:

$$
\begin{aligned}
x_1(t=0) &= 2.09785 \cdot 10^{-3}\,\mathrm{kg},\\
x_2(t=0) &= 1.14592 \cdot 10^{-3}\,\mathrm{kg},\\
x_3(t=0) &= 1.87539 \cdot 10^{-4}\,\mathrm{kg},\\
x_4(t=0) &= 1.43240 \cdot 10^{-3}\,\mathrm{kg},\\
x_5(t=0) &= 5. \qquad (2.75)
\end{aligned}
$$

2.3.1 Dynamic behaviour

In order to test the dynamic behaviour of the PEM fuel cell model, different steps of the input current are chosen. Figure 2.5 shows the simulation of states and output tp the corresponding input signal. The transient effects of the mass flow in the cathode and anode and those of the downstream PT1 element on the membrane humidity can be seen well, increasing or decreasing slowly after input steps.

Comparing the simulation results of the PEMFC model with those of Pukrsuhpan [6], similarities can be observed. In particular, the behaviour of the output voltage U_{st} and the oxygen mass $m_{\mathrm{O_2,ca}}$ on the steps of the stack current I_{st} is comparable to the work of Pukrushpan. The effects of the downstream PT1 element can be seen in the output voltage. Due to this first-order lag element, the fuel cell needs some time until the voltage adjusts after input steps. The mass of hydrogen in the anode hardly shows any dynamic behaviour, as the supply of the fuel is solved with a P-controller and thus exactly the right amount of hydrogen is supplied.
The fuel cell model represents the basic system behaviour well and can thus be used as a basis for the moving horizon state observer.

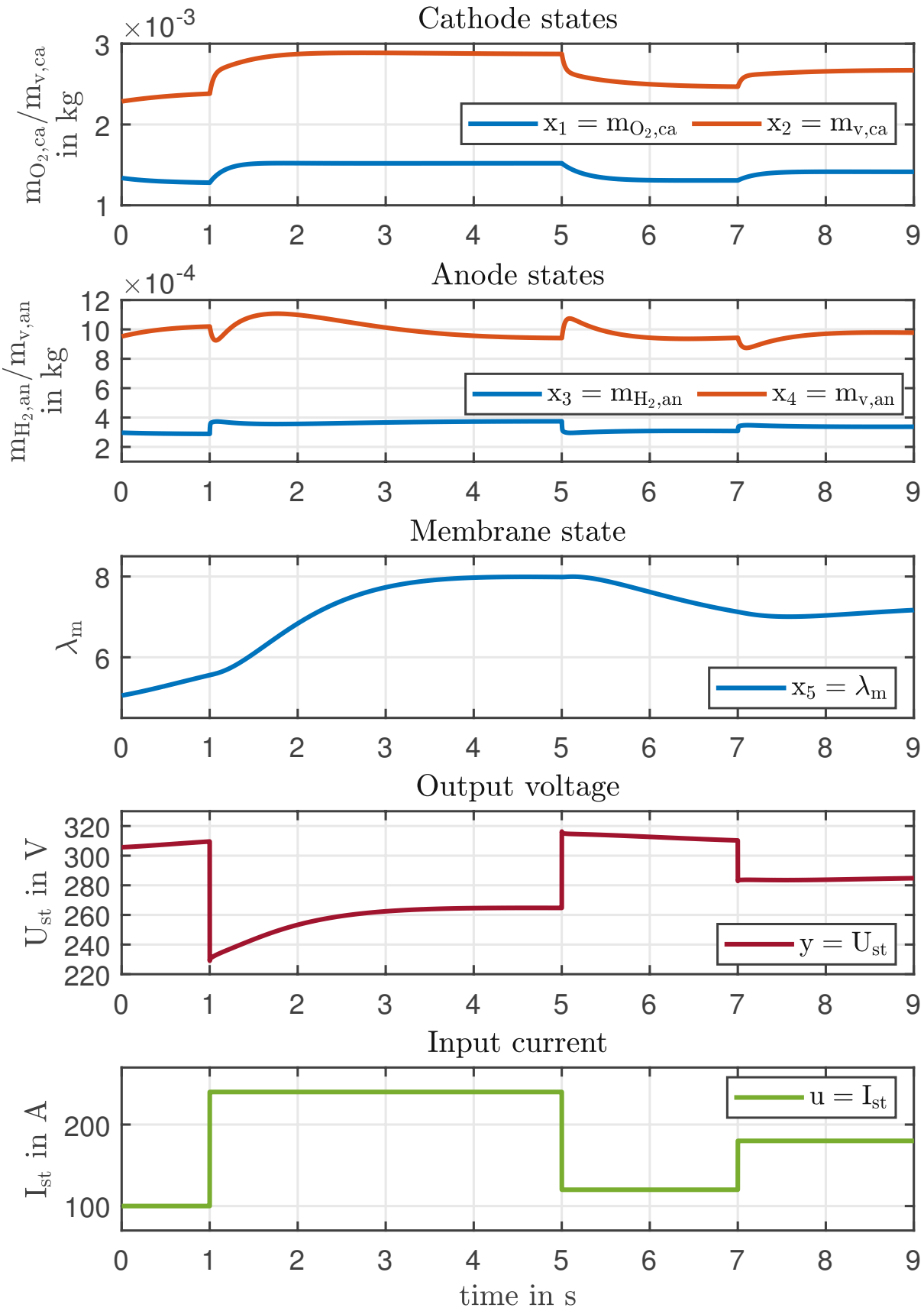

Figure 2.5: Simulation of the PEMFC Model

2.3.2 Polarization curve

The polarisation curve provides information about the performance and characteristics of a fuel cell. This diagram represents the steady-state relationship between cell voltage $V_{\text{cell}}\,(\text{V})$ and the current density $i\,(\text{A/cm}^2)$. The current is normalised to allow the comparison of fuel cells of different sizes or power. This graph describes the voltage drop or the voltage deviation from the ideal (thermodynamic) fuel cell voltage E_0 with increasing current.
In [1] the $(V-i)$-curve is divided into three areas along the x-axis, as can be seen in Figure 2.6. In the low current density range, the activation losses are mainly responsible for the voltage drop, which is shown in Figure 2.7a. For this reason, the area is also called the activation region. In the ohmic region (the middle region), the voltage drop is mainly caused by the approximately linearly increasing ohmic voltage drop V_{ohm}, which is shown in Figure 2.7b. The voltage drop V_{conc}, which results from the concentration differences of the reactants, dominates the last section. This behaviour is shown in Figure 2.7c. For this reason, this section is also called the mass transport region.

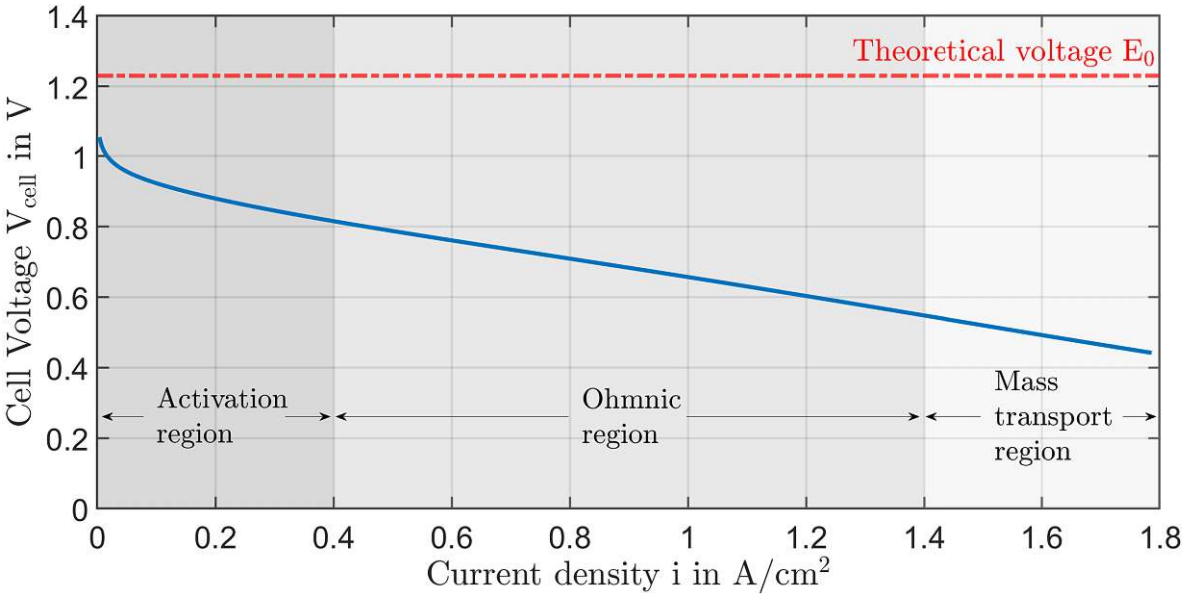

Figure 2.6: Polarization curve

The figure 2.7a to 2.7c show the polarisation curve split into its 3 components, which coincide with the expected theoretical results from [1]. The properties of the static relationship between current and voltage are very similar to the two polarisation curves in [6, 1]. Only in the range of higher current densities does the model deviate from

the references. This deviation can be explained because the fuel cell model is not parametrised for a specific fuel cell stack. In addition, parameter values from different sources were used for the simulation. However, since this model is mainly intended to validate the concept of the moving horizon estimation and not calibrated to an existing stack, this deviation will not be discussed further.

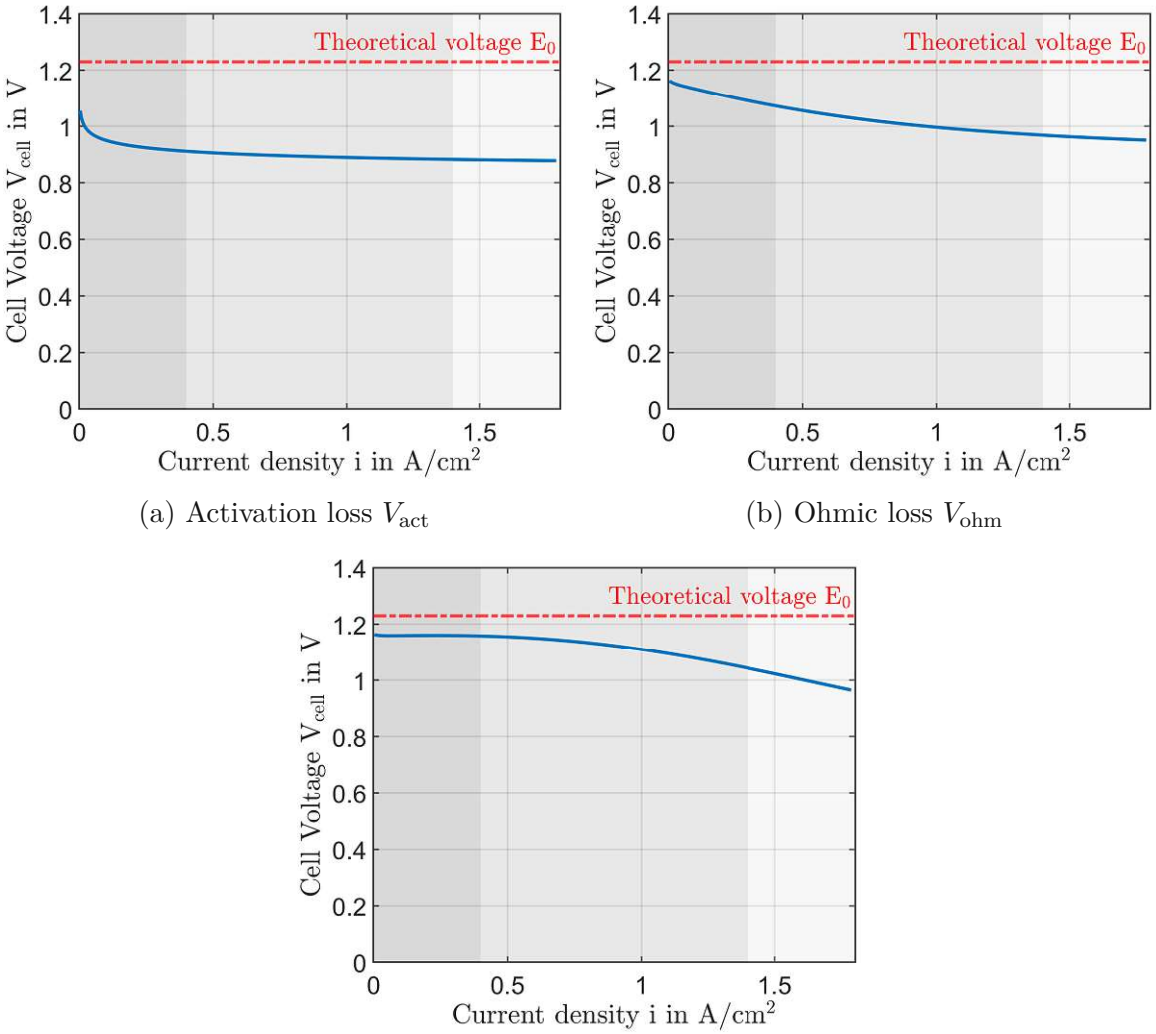

(a) Activation loss V_{act}

(b) Ohmic loss V_{ohm}

(c) Concentration loss V_{conc}

Figure 2.7: Polarisation curve divided into its components

Chapter 3

Moving horizon state estimation

3.1 Introduction to state observers

To be able to guarantee stable and efficient operation of the fuel cell system, states like the membrane humidity of the fuel cell must be constantly monitored. Since the relevant internal states cannot be measured, so-called observers are used. Observers use models and available measurements to reconstruct the non-measurable or non-measured quantities. This important model-based instrument from control engineering is therefore intended to support the fuel cell's operation, especially model-based control, and can be used to indicate undesired behaviour at an early stage.
State observers, especially nonlinear state observers, are a wide-ranging and complex subject. Each individual type of observer represents a separate field of research. For linear systems with Gaussian noise signals as process and measurement noise, the Kalman filter (KF) for example is the optimal state observer [51].
Probably the best known and widely used nonlinear observer concept is the extended Kalman filter. The EKF represents the nonlinear version of the KF, linearised around the current state estimate. In [36] the most common nonlinear forms of observers are compared.
In this thesis, the concept of the moving horizon state estimation will be applied, derived and implemented on the fuel cell system presented in Chapter 2. State estimation with a moving horizon is also sometimes referred to as receding horizon estimation. Compared to the optimal observer, not all available information is used, but instead, an attempt is made to combine the information of the past output measurements in a limited horizon. The information from past measurements is to be included in the state estimation to increase the quality of the estimation.
In MHE, the initial state of a dynamic system and the disturbances acting on the system are estimated for using a limited time horizon in the past. The state estimation is based on minimising the discrepancy between the measured values of the system output

and the output values calculated with the model. This estimation requires the solution of a dynamic optimisation task at each time step and is performed recurrently at discrete points in time. The optimisation task to be solved is written for a time horizon that begins in the past and ends at the current time. For the recurrent estimation, this horizon must be moved forward in time.

3.1.1 History of MHE

The origin of state observers dates far back in the history. The development of the first methods was influenced by very prominent scientists such as Gauss, Lengendre and Maxwell [37]. The least-squares method represents the first approach that returns the optimal estimate from a noisy measurement signal. This approach was developed as scientists searched for solutions to navigate the world's oceans.
However, systematic research on state estimators did not begin until the 1940s. Rudolph Kalman made a breakthrough in state observation in 1960 with the Kalman filter named after him. Even today, the Kalman filter is used in many areas such as space and aircraft navigation, GPS, the chemical process industry, economics, weather and air quality forecasting, communication networks and much more [37]. The connection between the Kalman filter and optimisation was demonstrated by Bryson in 1963 [38].
Although the computational implementation of a real-time solution was not yet possible, the first papers on moving horizon estimation were published in the 1960s. This limitation also led to the development of recursive methods for solving the optimisation tasks. [39] makes the approximation that extends the Kalman filter and linearises the nonlinear model around the current estimated state using a first-order Taylor series. With the increasing availability of powerful computers, the development of optimisation-based control engineering methods, such as the moving horizon state estimation, was advanced. Jang [40] published the first unconstrained nonlinear MHE, but he neglected the process noise. Jang's work has been taken as a basis and extended by many researchers. For example, [41] investigated the moving horizon strategy for state estimation as an extension to model predictive control. Subsequently, intensive research was carried out in the field of MHE to gain a better understanding of the method and to be able to make statements on stability [42, 43]. Robertson [44, 45] investigated the effects of constraints and the probabilistic interpretation, respectively. Rao and Rawlings published work on stability for both the linear constrained MHE [46], and the nonlinear constrained MHE [16]. Especially the paper [16] will serve as a basis for the derivation of the MHE in the further course of this work.

3.1.2 Advantages of the MHE

In addition to the very computational effort that results from the dynamic optimisation task at each time step, moving horizon state estimation has several advantages. The MHE is well suited for systems that have the following properties [17]:

- systems whose states are subject to constraints
- nonlinear systems
- disturbances and noise signals do not need to have specific stochastic properties
- systems where the initial state $\boldsymbol{x}(0)$ must be reconstructed.

All these advantages have to be weighed, since implementing the estimation procedure with the corresponding solution procedure for the optimisation task for the first time means a considerable additional effort compared to simpler methods such as the extended Kalman filter.

3.1.3 Observability

Before designing a state observer, one must first check whether the states of the desired system are observable. Observability in general means that one can uniquely reconstruct the modelled states $\boldsymbol{x}$ of the system with the help of the measured outputs $\boldsymbol{y}$. In general terms, observability can be defined as follows [47]

Definition 3.1: Observability

A system

$$\begin{aligned} \dot{\boldsymbol{x}} &= \boldsymbol{f}(\boldsymbol{x}, \boldsymbol{u}) \qquad \text{with } \boldsymbol{x}(t_0) = \boldsymbol{x_0} \\ \boldsymbol{y} &= \boldsymbol{h}(\boldsymbol{x}, \boldsymbol{u}) \end{aligned}$$

Let $\boldsymbol{x} \in D_{\boldsymbol{x}} \subseteq \mathbb{R}^n$ and $\boldsymbol{u} \in C_{\boldsymbol{u}} \subseteq C^{n-1}$ be defined and let $\boldsymbol{y} \in \mathbb{R}^r$. If then all initial vectors $\boldsymbol{x}_0 \in D_{\boldsymbol{x}}$ from the knowledge of $\boldsymbol{u}(t)$ and $\boldsymbol{y}(t)$ are in the time intervall $[t_0, t_1 < \infty]$ can be uniquely determined for all $\boldsymbol{u} \in C_{\boldsymbol{u}}$, then the system is called observable.

Here C^{n-1} is the space of $(n-1)$ - times continuously differentiable vector functions and the function $\boldsymbol{u}(t)$.

The observability of the fuel cell system from Chapter 2 is checked with a linear criterion. As already mentioned, the mass of the nitrogen $m_{\mathrm{H_2,ca}}$ is modelled algebraically since it has no influence on the output. Thus, it would lead to a model with non-full rank of the observability matrix based on the Kalman criterion. This observability check criterion for linear systems is defined as follows:

Definition 3.2: Kalman's observability criterion

A system is fully observable, if the observability matrix $\boldsymbol{S}_B$ has full rank

$$\boldsymbol{S}_B = \begin{bmatrix} \boldsymbol{C} \\ \boldsymbol{CA} \\ \boldsymbol{CA}^2 \\ \vdots \\ \boldsymbol{CA}^{n-1} \end{bmatrix} \qquad \operatorname{rank}(\boldsymbol{S}_B) = n. \tag{3.1}$$

n represents the number of states of the system. The observability matrix of the PEM fuel cell system around the starting point $\boldsymbol{x}_0$ has full rank and thus all states of the system are fully reconstructable by measuring the output voltage $y = V_{st}$.

3.2 Probabilistic derivation of the MHE

The Moving Horizon Estimator attempts to reconstruct the evolution of the states of the system $\{\boldsymbol{x}(t); t > 0\}$ at time T using the measured outputs $\{\boldsymbol{y}_0, \boldsymbol{y}_1, \ldots, \boldsymbol{y}_T\}$. It is assumed that the system has the following non-linear discrete-time representation

$$\boldsymbol{x}_{k+1} = f(\boldsymbol{x}_k, \boldsymbol{u}_k) + \boldsymbol{w}_k \tag{3.2}$$

$$\boldsymbol{y}_k = h(\boldsymbol{x}_k, \boldsymbol{u}_k) + \boldsymbol{v}_k \tag{3.3}$$

$$\begin{aligned} &\boldsymbol{x} \in \mathbb{R}^{n\times 1} \qquad \boldsymbol{u} \in \mathbb{R}^{m\times 1} \qquad \boldsymbol{y} \in \mathbb{R}^{p\times 1} \\ &\boldsymbol{w} \in \mathbb{R}^{n\times 1} \qquad \boldsymbol{v} \in \mathbb{R}^{p\times 1} \\ &\boldsymbol{w} \sim \mathcal{N}(\boldsymbol{0}, \boldsymbol{Q}) \quad \boldsymbol{v} \sim \mathcal{N}(\boldsymbol{0}, \boldsymbol{R}) \end{aligned}$$

where k denotes discrete time, $\boldsymbol{v}$ is a normally distributed mean-free process noise with variance $\boldsymbol{R}$, $\boldsymbol{w}$ is a normally distributed mean-free process noise with variance $\boldsymbol{Q}$, n number of states, m number of inputs and p number of outputs.

In the following section, the problem of state estimation is formulated from the perspective of probability theory. The derivation is analogous to the work by Rao [43]. Further probabilistic interpretation can be found in [39, 48, 49, 17], which are also used in this thesis.
In [43], the evolution of the states is modelled as a Markov process, which is equivalent to the process perturbations $\boldsymbol{w}_k$ being independent. Since the output measurements $\{\boldsymbol{y}_0, \boldsymbol{y}_1, \ldots, \boldsymbol{y}_T\}$ depend on the states $\{\boldsymbol{x}_0, \boldsymbol{x}_1, \ldots, \boldsymbol{x}_T\}$, respectively correlate, the conditional probability density function is the property of interest in this observer form

$$p\left(\boldsymbol{x}_0, \boldsymbol{x}_1, \ldots, \boldsymbol{x}_T \mid \boldsymbol{y}_0, \boldsymbol{y}_1 \ldots, \boldsymbol{y}_T\right). \tag{3.4}$$

The optimal estimate at time k is now obtained by maximising the conditional probability density function (3.4), yielding a maximum a posteriori estimator (MAP)

$$\{\hat{\boldsymbol{x}}_{0|T}, \hat{\boldsymbol{x}}_{1|T}, \ldots, \hat{\boldsymbol{x}}_{T|T}\} = \arg \max_{\boldsymbol{x}_0, \{\boldsymbol{w}\}_0^{T-1}} p\left(\boldsymbol{x}_0, \boldsymbol{x}_1, \ldots, \boldsymbol{x}_T \mid \boldsymbol{y}_0, \boldsymbol{y}_1, \ldots, \boldsymbol{y}_T\right). \tag{3.5}$$

$\hat{\boldsymbol{x}}_{i|j}$ is the estimated state $\boldsymbol{x}_i$ calculated at time j and $\{\boldsymbol{w}\}_0^{T-1}$ is the simplified notation for the process disturbances $\{\boldsymbol{w}_0, \boldsymbol{w}_1, \ldots, \boldsymbol{w}_{T-1}\}$. In order to solve (3.5), an expression for the conditional probability density function (3.4) must be found. Analogous to [39], one can exploit the Markov properties and express the joint probability of the states as follows

$$p\left(\boldsymbol{x}_0, \boldsymbol{x}_1, \ldots, \boldsymbol{x}_T\right) = p_{\boldsymbol{x}_0}(\boldsymbol{x}_0) \prod_{k=0}^{T-1} p_{\boldsymbol{w}_k}\left(\boldsymbol{x}_{k+1} - \boldsymbol{f}(\boldsymbol{x}_k, \boldsymbol{u}_k)\right) \tag{3.6}$$

where $p_{\boldsymbol{x}_0}$ contains the prior information about the state $\boldsymbol{x}_0$ and $p_{\boldsymbol{w}_k}$ the probability density function of the process disturbance. Assuming that the measurement noise $\boldsymbol{v}_k$ is independent, the following relationship can be written, taking into account equation (3.3)

$$p\left(\boldsymbol{y}_0, \boldsymbol{y}_1, \ldots, \boldsymbol{y}_T | \boldsymbol{x}_0, \boldsymbol{x}_1, \ldots, \boldsymbol{x}_T\right) = \prod_{k=0}^{T} p_{\boldsymbol{v}_k}\left(\boldsymbol{y}_k - \boldsymbol{h}(\boldsymbol{x}_k, \boldsymbol{u}_k)\right) \tag{3.7}$$

where $p_{\boldsymbol{v}_k}$ is the probability density function of the measurement noise. If Bayes' theorem is now applied, the following expression for the conditional probability density function is obtained

$$p\left(\boldsymbol{x}_0, \boldsymbol{x}_1, \ldots, \boldsymbol{x}_T | \boldsymbol{y}_0, \boldsymbol{y}_1, \ldots, \boldsymbol{y}_T\right) \propto$$
$$p_{\boldsymbol{x}_0}(\boldsymbol{x}_0) \prod_{k=0}^{T} p_{\boldsymbol{v}_k}\left(\boldsymbol{y}_k - \boldsymbol{h}(\boldsymbol{x}_k, \boldsymbol{u}_k)\right) \cdot \prod_{k=0}^{T-1} p_{\boldsymbol{w}_k}\left(\boldsymbol{x}_{k+1} - \boldsymbol{f}(\boldsymbol{x}_k, \boldsymbol{u}_k)\right). \tag{3.8}$$

If one applies the logarithm to equation (3.5), it can be formulated as follows due to the properties of the logarithm

$$\begin{aligned}
&\arg \max_{\boldsymbol{x}_0, \{\boldsymbol{w}\}_0^{T-1}} p\left(\boldsymbol{x}_0, \boldsymbol{x}_1, \ldots, \boldsymbol{x}_T \mid \boldsymbol{y}_0, \boldsymbol{y}_1, \ldots, \boldsymbol{y}_T\right) \\
&= \max_{\boldsymbol{x}_0, \{\boldsymbol{w}\}_0^{T-1}} \log p\left(\boldsymbol{x}_0, \boldsymbol{x}_1, \ldots, \boldsymbol{x}_T \mid \boldsymbol{y}_0, \boldsymbol{y}_1, \ldots, \boldsymbol{y}_T\right) \\
&= \arg \max_{\boldsymbol{x}_0, \{\boldsymbol{w}\}_0^{T-1}} \log p_{\boldsymbol{x}_0}(\boldsymbol{x}_0) + \sum_{k=0}^{T} \log p_{\boldsymbol{v}_k}\left(\boldsymbol{y}_k - \boldsymbol{h}(\boldsymbol{x}_k, \boldsymbol{u}_k)\right) + \\
&\quad \sum_{k=0}^{T-1} \log p_{\boldsymbol{w}_k}\left(\boldsymbol{x}_{k+1} - \boldsymbol{f}(\boldsymbol{x}_k, \boldsymbol{u}_k)\right)
\end{aligned} \tag{3.9}$$

By assuming that the probability density functions $p_{\boldsymbol{x}_0}$, $p_{\boldsymbol{w}_k}$ and $p_{\boldsymbol{v}_k}$ are normally distributed with the covariances $\boldsymbol{P}_0$, $\boldsymbol{Q}$ and $\boldsymbol{R}$, the maximisation of the probability density function in equation (3.9) can be transformed into the following minimisation task

$$\begin{aligned}
&\arg \max_{\boldsymbol{x}_0, \{\boldsymbol{w}\}_0^{T-1}} p\left(\boldsymbol{x}_0, \boldsymbol{x}_1, \ldots, \boldsymbol{x}_T \mid \boldsymbol{y}_0, \boldsymbol{y}_1, \ldots, \boldsymbol{y}_T\right) = \\
&\quad \arg \min_{\boldsymbol{x}_0, \{\boldsymbol{w}\}_0^{T-1}} \|\boldsymbol{x}_0 - \overline{\boldsymbol{x}}_0\|^2_{\boldsymbol{P}_0^{-1}} + \sum_{k=0}^{T} \|\boldsymbol{y}_k - \boldsymbol{h}(\boldsymbol{x}_k, \boldsymbol{u}_k)\|^2_{\boldsymbol{R}^{-1}} \\
&\quad + \sum_{k=0}^{T-1} \|\boldsymbol{x}_{k+1} - \boldsymbol{f}(\boldsymbol{x}_k, \boldsymbol{u}_k)\|^2_{\boldsymbol{Q}^{-1}}
\end{aligned} \tag{3.10}$$

where $\|\boldsymbol{z}\| = \boldsymbol{z}^T \boldsymbol{A} \boldsymbol{z}$ and $\overline{\boldsymbol{x}}$ is the mean of density $p_{\boldsymbol{x}_0}$. The optimisation task (3.10) is also called the full information (FI) problem. The state estimation task at time T can be rewritten into the following mathematical problem

$$\min_{\boldsymbol{x}_0, \{\boldsymbol{w}\}_0^{T-1}} \Phi_T\left(\boldsymbol{x}_0, \{\boldsymbol{w}\}_0^{T-1}\right)$$

subject to

$$\begin{aligned}
\boldsymbol{x}_{k-1} &= \boldsymbol{f}\left(\boldsymbol{x}_k, \boldsymbol{u}_k\right) + \boldsymbol{w}_k \qquad \forall k = 0, \ldots, T-1 \\
\boldsymbol{y}_k &= \boldsymbol{h}\left(\boldsymbol{x}_k, \boldsymbol{u}_k\right) + \boldsymbol{v}_k \qquad \forall k = 0, \ldots, T
\end{aligned}$$

where

$$\Phi_T\left(\boldsymbol{x}_0, \{\boldsymbol{w}\}_0^{T-1}\right) = \sum_{k=0}^{T} \|\boldsymbol{v}\|^2_{\boldsymbol{R}^{-1}} + \sum_{k=0}^{T-1} \|\boldsymbol{w}\|^2_{\boldsymbol{Q}^{-1}} + \|\boldsymbol{x}_0 - \overline{\boldsymbol{x}}_0\|^2_{\boldsymbol{P}_0^{-1}} \tag{3.11}$$

However, this formulation is not practically for an online implementation since the size of the problem grows with time. To realise the possibility of an online implementation and to limit the size of the optimisation task, Φ_T is divided into the following two sections

$$\begin{aligned}\Phi_T\left(\boldsymbol{x}_0, \{\boldsymbol{w}\}_0^{T-1}\right) = &\sum_{k=T-N_o}^{T} \|\boldsymbol{v}\|^2_{\boldsymbol{R}^{-1}} + \sum_{k=T-N_o}^{T-1} \|\boldsymbol{w}\|^2_{\boldsymbol{Q}^{-1}} \\ &+ \sum_{k=0}^{T-N_o-1} \|\boldsymbol{v}\|^2_{\boldsymbol{R}^{-1}} + \sum_{k=0}^{T-N_o-1} \|\boldsymbol{w}\|^2_{\boldsymbol{Q}^{-1}} \|\boldsymbol{x}_0 - \overline{\boldsymbol{x}}_0\|^2_{\boldsymbol{P}_0^{-1}}\end{aligned} \tag{3.12}$$

where N_o is the length of the observed horizon. The first expression

$$\sum_{k=T-N_\mathrm{o}}^{T} \|\boldsymbol{v}\|^2_{\boldsymbol{R}^{-1}} + \sum_{k=T-N_\mathrm{o}}^{T-1} \|\boldsymbol{w}\|^2_{\boldsymbol{Q}^{-1}}$$

depends on the state at the beginning of the horizon $\boldsymbol{x}_{T-N_\mathrm{o}}$, the process disturbances occurring in the section $\{\boldsymbol{w}\}_{T-N_\mathrm{o}}^{T-1}$ and the sequence of measured outputs $\{\boldsymbol{y}\}_{T-N_\mathrm{o}}^{T}$. The optimality principle allows the state observation to be performed on a fixed horizon. Thus, the optimisation task originally extended over the entire data can be reduced to the following mathematical problem

$$\min_{\boldsymbol{x}_{T-N_\mathrm{o}}, \{\boldsymbol{w}\}_{T-N_\mathrm{o}}^{T-1}} \quad \sum_{k=T-N_\mathrm{o}}^{T} \|\boldsymbol{v}\|^2_{\boldsymbol{R}^{-1}} + \sum_{k=T-N_\mathrm{o}}^{T-1} \|\boldsymbol{w}\|^2_{\boldsymbol{Q}^{-1}} + Z_{T-N_\mathrm{o}}\left(\boldsymbol{x}_{T-N_\mathrm{o}}\right) \tag{3.13}$$

with the system and output equation as constraints. This formulation represents the basic structure of the moving horizon estimator, which uses only the last $N_\mathrm{o}+1$ output measurement to estimate the current state $\boldsymbol{x}_T$. Z_{T-N_o} represent the arrival cost (AC). The AC are a fundamental part of the MHE, since it transforms the unconstrained full information problem into a constrained optimisation task. By means of the arrival cost term, all the information that is not included in the optimisation horizon is summarised. The influence of the initial measurements $\{\boldsymbol{y}\}_0^{T-N_\mathrm{o}}$ on the state at the beginning of the horizon $\boldsymbol{x}_{T-N_\mathrm{o}}$ are included in the state estimate in compressed form Z_{T-N_o}. From a probabilistic point of view, the arrival cost can also be interpreted as

the conditional probability density function $p(\boldsymbol{x}_{k-N_\mathrm{o}}|\boldsymbol{y}_o, \boldsymbol{y}_1, \ldots, \boldsymbol{y}_{k-N_\mathrm{o}})$. Proceeding in the same way as in the derivation of the FI problem, maximising the conditional probability $p(\boldsymbol{x}_{k-N_\mathrm{o}}|\boldsymbol{y}_o, \boldsymbol{y}_1, \ldots, \boldsymbol{y}_{k-N_\mathrm{o}})$ is equivalent to minimising the negative logarithm of $p(\boldsymbol{x}_{k-N_\mathrm{o}}|\boldsymbol{y}_o, \boldsymbol{y}_1, \ldots, \boldsymbol{y}_{k-N_\mathrm{o}})$. An exact calculation of the arrival costs Z_{T-N_o} is not possible, therefore the AC must be approximated. A very common assumption, as made in [16, 48], is that the conditional probability density function is approximated by a normal distribution $p(\boldsymbol{x}_{k-N_\mathrm{o}}|\boldsymbol{y}_o, \boldsymbol{y}_1, \ldots, \boldsymbol{y}_{k-N_\mathrm{o}}) \sim \mathcal{N}\left(\hat{\boldsymbol{x}}_{T-N_\mathrm{o}|T-N_\mathrm{o}}, \boldsymbol{P}_{T-N_\mathrm{o}}\right)$. In this case, the model is approximated by a first-order tailor series around the solution trajectory generated by the MHE $\{\hat{\boldsymbol{x}}\}_0^{T-N_\mathrm{o}}$. The covariance matrix $\boldsymbol{P}_{T-N_\mathrm{o}}$ is updated analogously to the EKF [16].

Thus, the following optimisation problem results for the state estimation at time T

$$\hat{\boldsymbol{x}}_{T|T} = \boldsymbol{f}\left(\hat{\boldsymbol{x}}_{k-N_\mathrm{o}|T}, \{\hat{\boldsymbol{w}}\}_{T-N_\mathrm{o}|T}^{T-1|T}\right) = \tag{3.14}$$

$$\min_{\boldsymbol{x}_{T-N_\mathrm{o}}, \{\boldsymbol{w}\}_{T-N_\mathrm{o}}^{T-1}} \quad \|\boldsymbol{x}_{T-N_\mathrm{o}} - \hat{\boldsymbol{x}}_{k-N_\mathrm{o}|k-N_\mathrm{o}}\|^2_{\boldsymbol{P}_{\boldsymbol{k-N_\mathrm{o}}}^{-1}} + \sum_{k=T-N_\mathrm{o}}^{T} \|\boldsymbol{v}\|^2_{\boldsymbol{R}^{-1}} + \sum_{k=T-N_\mathrm{o}}^{T-1} \|\boldsymbol{w}\|^2_{\boldsymbol{Q}^{-1}}$$

subject to

$$\begin{aligned} \boldsymbol{x}_{k-1} &= \boldsymbol{f}\left(\boldsymbol{x}_k, \boldsymbol{u}_k\right) + \boldsymbol{w}_k \qquad \forall k = T - N_\mathrm{o}, \ldots, T-1 \\ \boldsymbol{y}_k &= \boldsymbol{h}\left(\boldsymbol{x}_k, \boldsymbol{u}_k\right) + \boldsymbol{v}_k \qquad \forall k = T - N_\mathrm{o}, \ldots, T. \end{aligned}$$

By minimising the cost function, one obtains the estimated state at the beginning of the horizon $\hat{\boldsymbol{x}}_{T-N_\mathrm{o}|T}$ and the estimated process disturbances in the horizon $\{\hat{\boldsymbol{w}}\}_{T-N_\mathrm{o}|T}^{T-1|T}$. Using the results of the optimisation task and the system equation (3.2), the estimate of the current state $\hat{\boldsymbol{x}}_{T|T}$ can be calculated. The weighting matrix for the arrival cost is determined by solving the Riccati equation

$$\boldsymbol{P}_{j+1} = \boldsymbol{Q} + \boldsymbol{A}_j \boldsymbol{P}_j \boldsymbol{A}_j^T - \boldsymbol{A}_j \boldsymbol{P}_j \boldsymbol{C}_j^T \left(\boldsymbol{R} + \boldsymbol{C}_j \boldsymbol{P}_j \boldsymbol{C}_j^T\right)^{-1} \boldsymbol{C}_j \boldsymbol{P}_j \boldsymbol{A}_j^T \tag{3.15}$$

where j denotes discrete time and P_0 is the initial condition.

Stability investigations are not carried out in this work, as it would exceed the scope of this thesis, but proofs of the stability of the Moving Horizon Estimator concept are presented in [16].

3.3 Successive linearisation

The moving horizon estimator is to be implemented using the method of successive linearisation. With this method, the offsets δ_x and δ_y resulting from linearisation are

taken into account in the system equation as well as in the output equation. The system matrices are created by linearising around the solution trajectory $\hat{\boldsymbol{x}}$ generated by the MHE. The linearisation at time k is based on the optimal estimate $\hat{\boldsymbol{x}}_{k|k}$ at that time.

$$\boldsymbol{x}_{k+1} = \boldsymbol{A}_k \boldsymbol{x}_k + \boldsymbol{B}_k \boldsymbol{u}_k + \boldsymbol{\delta}_{\mathrm{x},k} + \boldsymbol{w}_k \tag{3.16}$$

$$\boldsymbol{y}_k = \boldsymbol{C}_k \boldsymbol{x}_k + \boldsymbol{D}_k \boldsymbol{u}_k + \boldsymbol{\delta}_{\mathrm{y},k} + \boldsymbol{v}_k \tag{3.17}$$

$$\boldsymbol{A}_k = \boldsymbol{A}_{k|k} \coloneqq \left.\frac{\partial \boldsymbol{f}(\boldsymbol{x},\, \boldsymbol{u})}{\partial \boldsymbol{x}}\right|_{\substack{\hat{\boldsymbol{x}}_{k|k} \\ \boldsymbol{u}_k}} \qquad \boldsymbol{B}_k = \boldsymbol{B}_{k|k} \coloneqq \left.\frac{\partial \boldsymbol{f}(\boldsymbol{x},\, \boldsymbol{u})}{\partial \boldsymbol{u}}\right|_{\substack{\hat{\boldsymbol{x}}_{k|k} \\ \boldsymbol{u}_k}}$$

$$\boldsymbol{C}_k = \boldsymbol{C}_{k|k} \coloneqq \left.\frac{\partial \boldsymbol{h}(\boldsymbol{x},\, \boldsymbol{u})}{\partial \boldsymbol{x}}\right|_{\substack{\hat{\boldsymbol{x}}_{k|k} \\ \boldsymbol{u}_k}} \qquad \boldsymbol{D}_k = \boldsymbol{D}_{k|k} \coloneqq \left.\frac{\partial \boldsymbol{h}(\boldsymbol{x},\, \boldsymbol{u})}{\partial \boldsymbol{u}}\right|_{\substack{\hat{\boldsymbol{x}}_{k|k} \\ \boldsymbol{u}_k}}$$

$$\boldsymbol{\delta}_{\mathrm{x},k} = \boldsymbol{\delta}_{\mathrm{x},k|k} \coloneqq \boldsymbol{f}\left(\hat{\boldsymbol{x}}_{k|k}, \boldsymbol{u}_k\right) - \boldsymbol{A}_k \hat{\boldsymbol{x}}_{k|k} - \boldsymbol{B}_k \boldsymbol{u}_k$$

$$\boldsymbol{\delta}_{\mathrm{y},k} = \boldsymbol{\delta}_{\mathrm{y},k|k} \coloneqq \boldsymbol{h}\left(\hat{\boldsymbol{x}}_{k|k}, \boldsymbol{u}_k\right) - \boldsymbol{C}_k \hat{\boldsymbol{x}}_{k|k} - \boldsymbol{D}_k \boldsymbol{u}_k.$$

3.4 Derivation of the MHE formulation

In the following chapter, the concrete implementation of the moving horizon state estimation concept is derived with the help of successive linearisation. The observation horizon extends from the current time k and N_o time steps back into the past. In principle, the MHE can be implemented as a filter and as a predictive observer [17]. The only difference between these two forms is whether the current measurement of the output $\boldsymbol{y}_k$ is still used to estimate the state $\hat{\boldsymbol{x}}_k$. The MHE in this thesis is implemented as a filter, i.e. $N_\mathrm{o} + 1$ output measurements are used to estimate the current state. In the first step, the system equations for the entire horizon in which the optimisation task is formulated are written down as a function of the optimisation variables $\boldsymbol{x}_{k-N_\mathrm{o}}$ and $\{\boldsymbol{w}\}_{k-N_\mathrm{o}}^{k-1}$.

$$
\begin{aligned}
\boldsymbol{x}_{k-N_\mathrm{o}+1|k} &= \boldsymbol{A}_{k-N_\mathrm{o}}\boldsymbol{x}_{k-N_\mathrm{o}} + \boldsymbol{B}_{k-N_\mathrm{o}}\boldsymbol{u}_{k-N_\mathrm{o}} + \boldsymbol{\delta}_{\mathrm{x},k-N_\mathrm{o}} + \boldsymbol{w}_{k-N_\mathrm{o}} \\
\boldsymbol{x}_{k-N_\mathrm{o}+2|k} &= \boldsymbol{A}_{k-N_\mathrm{o}+1}\boldsymbol{x}_{k-N_\mathrm{o}+1} + \boldsymbol{B}_{k-N_\mathrm{o}+1}\boldsymbol{u}_{k-N_\mathrm{o}+1} + \boldsymbol{\delta}_{\mathrm{x},k-N_\mathrm{o}+1} + \boldsymbol{w}_{k-N_\mathrm{o}+1} \\
&= \boldsymbol{A}_{k-N_\mathrm{o}+1}\boldsymbol{A}_{k-N_\mathrm{o}}\boldsymbol{x}_{k-N_\mathrm{o}} + \boldsymbol{A}_{k-N_\mathrm{o}+1}\boldsymbol{B}_{K-N_\mathrm{o}}\boldsymbol{u}_{k-N_\mathrm{o}} + \boldsymbol{B}_{k-N_\mathrm{o}+1}\boldsymbol{u}_{k-N_\mathrm{o}+1} \\
&\quad + \boldsymbol{A}_{k-N_\mathrm{o}+1}\boldsymbol{\delta}_{\mathrm{x},k-N_\mathrm{o}} + \boldsymbol{\delta}_{\mathrm{x},k-N_\mathrm{o}+1} + \boldsymbol{A}_{k-N_\mathrm{o}+1}\boldsymbol{w}_{k-N_\mathrm{o}} + \boldsymbol{w}_{k-N_\mathrm{o}+1} \\
&\vdots \\
\boldsymbol{x}_{k|k} &= \left(\prod_{i=k-1}^{k-N_\mathrm{o}} \boldsymbol{A}_i\right)\boldsymbol{x}_{k-N_\mathrm{o}} + \left(\prod_{i=k-1}^{k-N_\mathrm{o}+1} \boldsymbol{A}_i\right)\boldsymbol{B}_{k-N_\mathrm{o}}\boldsymbol{u}_{k-N_\mathrm{o}} \\
&\quad + \left(\prod_{i=k-1}^{k-N_\mathrm{o}+2} \boldsymbol{A}_i\right)\boldsymbol{B}_{k-N_\mathrm{o}+1}\boldsymbol{u}_{k-N_\mathrm{o}+1} + \ldots + \boldsymbol{A}_{k-1}\boldsymbol{B}_{k-2}\boldsymbol{u}_{k-2} + \boldsymbol{B}_{k-1}\boldsymbol{u}_{k-1} \\
&\quad + \left(\prod_{i=k-1}^{k-N_\mathrm{o}+1} \boldsymbol{A}_i\right)\boldsymbol{w}_{k-N_\mathrm{o}} + \left(\prod_{i=k-1}^{k-N_\mathrm{o}+2} \boldsymbol{A}_i\right)\boldsymbol{w}_{k-N_\mathrm{o}+1} \ldots + \boldsymbol{A}_{k-1}\boldsymbol{w}_{k-2} + \boldsymbol{w}_{k-1} \\
&\quad + \left(\prod_{i=k-1}^{k-N_\mathrm{o}+1} \boldsymbol{A}_i\right)\boldsymbol{\delta}_{\mathrm{x},k-N_\mathrm{o}} + \left(\prod_{i=k-1}^{k-N_\mathrm{o}+2} \boldsymbol{A}_i\right)\boldsymbol{\delta}_{\mathrm{x},k-N_\mathrm{o}+1} \ldots + \boldsymbol{A}_{k-1}\boldsymbol{\delta}_{\mathrm{x},k-2} + \boldsymbol{\delta}_{\mathrm{x},k-1}
\end{aligned}
\tag{3.18}
$$

In the next step, the output equations of the observer for the horizon are formulated using the linearisation presented in Section 3.3.

$$
\begin{aligned}
\boldsymbol{y}_{k-N_\mathrm{o}+1|k} &= \boldsymbol{C}_{k-N_\mathrm{o}+1}\boldsymbol{x}_{k-N_\mathrm{o}+1} + \boldsymbol{D}_{k-N_\mathrm{o}+1}\boldsymbol{u}_{k-N_\mathrm{o}+1} + \boldsymbol{\delta}_{\mathrm{y},k-N_\mathrm{o}+1} + \boldsymbol{v}_{k-N_\mathrm{o}+1} \\
\boldsymbol{y}_{k-N_\mathrm{o}+2|k} &= \boldsymbol{C}_{k-N_\mathrm{o}+2}\boldsymbol{x}_{k-N_\mathrm{o}+2} + \boldsymbol{D}_{k-N_\mathrm{o}+2}\boldsymbol{u}_{k-N_\mathrm{o}+2} + \boldsymbol{\delta}_{\mathrm{y},k-N_\mathrm{o}+2} + \boldsymbol{v}_{k-N_\mathrm{o}+2} \\
&\vdots \\
\boldsymbol{y}_{k-1|k} &= \boldsymbol{C}_{k-1}\boldsymbol{x}_k + \boldsymbol{D}_{k-1}\boldsymbol{u}_{k-1} + \boldsymbol{\delta}_{\mathrm{y},k-1} + \boldsymbol{v}_{k-1} \\
\boldsymbol{y}_{k|k} &= \boldsymbol{C}_k\boldsymbol{x}_k + \boldsymbol{D}_k\boldsymbol{u}_k + \boldsymbol{\delta}_{\mathrm{y},k} + \boldsymbol{v}_k
\end{aligned}
\tag{3.19}
$$

Substituting the observer's system equations into the output equations yields the measured outputs as a function of the MHE's optimisation variables.

$$
\underbrace{\begin{bmatrix} \boldsymbol{y}_{k-N_\mathrm{o}+1|k} \\ \boldsymbol{y}_{k-N_\mathrm{o}+2|k} \\ \boldsymbol{y}_{k-N_\mathrm{o}+3|k} \\ \vdots \\ \boldsymbol{y}_{k-1|k} \\ \boldsymbol{y}_{k|k} \end{bmatrix}}_{(N_\mathrm{o}p\times 1)} = \underbrace{\begin{bmatrix} \boldsymbol{C}_{k-N_\mathrm{o}+1}\boldsymbol{A}_{k-N_\mathrm{o}} \\ \boldsymbol{C}_{k-N_\mathrm{o}+2}\boldsymbol{A}_{k-N_\mathrm{o}+1}\boldsymbol{A}_{k-N_\mathrm{o}} \\ \boldsymbol{C}_{k-N_\mathrm{o}+3}\boldsymbol{A}_{k-N_\mathrm{o}+2}\boldsymbol{A}_{k-N_\mathrm{o}+1}\boldsymbol{A}_{k-N_\mathrm{o}} \\ \vdots \\ \boldsymbol{C}_{k-1}\left(\prod_{i=k-2}^{k-N_\mathrm{o}} A_i\right) \\ \boldsymbol{C}_{k}\left(\prod_{i=k-1}^{k-N_\mathrm{o}} A_i\right) \end{bmatrix}}_{(N_\mathrm{o}p\times n)} \underbrace{\boldsymbol{x}_{k-N_\mathrm{o}}}_{n\times 1} +
$$

$$
\underbrace{\begin{bmatrix} \boldsymbol{C}_{k-N_\mathrm{o}+1}\boldsymbol{B}_{k-N_\mathrm{o}} & 0 & 0 & \cdots & 0 \\ \boldsymbol{C}_{k-N_\mathrm{o}+2}\boldsymbol{A}_{k-N_\mathrm{o}+1}\boldsymbol{B}_{k-N_\mathrm{o}} & 0 & 0 & \cdots & 0 \\ \boldsymbol{C}_{k-N_\mathrm{o}+3}\boldsymbol{A}_{k-N_\mathrm{o}+2}\boldsymbol{A}_{k-N_\mathrm{o}+1}\boldsymbol{B}_{k-N_\mathrm{o}} & \boldsymbol{C}_{k-N_\mathrm{o}+3}\boldsymbol{A}_{k-N_\mathrm{o}+2}\boldsymbol{B}_{k-N_\mathrm{o}+1} & 0 & \cdots & 0 \\ \vdots & & \ddots & & \vdots \\ \boldsymbol{C}_{k-1}\left(\prod_{i=k-2}^{k-N_\mathrm{o}+1} A_i\right)\boldsymbol{B}_{k-N_\mathrm{o}} & \boldsymbol{C}_{k-1}\left(\prod_{i=k-2}^{k-N_\mathrm{o}+2} A_i\right)\boldsymbol{B}_{k-N_\mathrm{o}+1} & \cdots & \boldsymbol{C}_{k-1}\boldsymbol{B}_{k-2} & 0 \\ \boldsymbol{C}_{k}\left(\prod_{i=k-1}^{k-N_\mathrm{o}+1} A_i\right)\boldsymbol{B}_{k-N_\mathrm{o}} & \boldsymbol{C}_{k}\left(\prod_{i=k-1}^{k-N_\mathrm{o}+2} A_i\right)\boldsymbol{B}_{k-N_\mathrm{o}+1} & \cdots & \boldsymbol{C}_{k}\boldsymbol{A}_{k-1}\boldsymbol{B}_{k-2} & \boldsymbol{C}_{k}\boldsymbol{B}_{k-1} \end{bmatrix}}_{(N_\mathrm{o}p\times N_\mathrm{o}m)}
$$

$$
\underbrace{\begin{bmatrix} \boldsymbol{u}_{k-N_\mathrm{o}} \\ \boldsymbol{u}_{k-N_\mathrm{o}+1} \\ \boldsymbol{u}_{k-N_\mathrm{o}+2} \\ \vdots \\ \boldsymbol{u}_{k-2} \\ \boldsymbol{u}_{k-1} \end{bmatrix}}_{(N_\mathrm{o}m\times 1)} + \underbrace{\begin{bmatrix} \boldsymbol{C}_{k-N_\mathrm{o}+1} & 0 & 0 & \cdots & 0 \\ \boldsymbol{C}_{k-N_\mathrm{o}+2}\boldsymbol{A}_{k-N_\mathrm{o}+1} & 0 & 0 & \cdots & 0 \\ \boldsymbol{C}_{k-N_\mathrm{o}+3}\boldsymbol{A}_{k-N_\mathrm{o}+2}\boldsymbol{A}_{k-N_\mathrm{o}+1} & \boldsymbol{C}_{k-N_\mathrm{o}+3}\boldsymbol{A}_{k-N_\mathrm{o}+2} & 0 & \cdots & 0 \\ \vdots & & \ddots & & \vdots \\ \boldsymbol{C}_{k-1}\left(\prod_{i=k-2}^{k-N_\mathrm{o}+1} A_i\right) & \boldsymbol{C}_{k-1}\left(\prod_{i=k-2}^{k-N_\mathrm{o}+2} A_i\right) & \cdots & \boldsymbol{C}_{k-1} & 0 \\ \boldsymbol{C}_{k}\left(\prod_{i=k-1}^{k-N_\mathrm{o}+1} A_i\right) & \boldsymbol{C}_{k}\left(\prod_{i=k-1}^{k-N_\mathrm{o}+2} A_i\right) & \cdots & \boldsymbol{C}_{k}\boldsymbol{A}_{k-1} & \boldsymbol{C}_{k} \end{bmatrix}}_{(N_\mathrm{o}p\times N_\mathrm{o}n)} \underbrace{\begin{bmatrix} \boldsymbol{w}_{k-N_\mathrm{o}} \\ \boldsymbol{w}_{k-N_\mathrm{o}+1} \\ \boldsymbol{w}_{k-N_\mathrm{o}+2} \\ \vdots \\ \boldsymbol{w}_{k-2} \\ \boldsymbol{w}_{k-1} \end{bmatrix}}_{(N_\mathrm{o}n\times 1)}
$$

$$
+ \underbrace{\begin{bmatrix} \boldsymbol{C}_{k-N_\mathrm{o}+1} & 0 & 0 & \cdots & 0 \\ \boldsymbol{C}_{k-N_\mathrm{o}+2}\boldsymbol{A}_{k-N_\mathrm{o}+1} & 0 & 0 & \cdots & 0 \\ \boldsymbol{C}_{k-N_\mathrm{o}+3}\boldsymbol{A}_{k-N_\mathrm{o}+2}\boldsymbol{A}_{k-N_\mathrm{o}+1} & \boldsymbol{C}_{k-N_\mathrm{o}+3}\boldsymbol{A}_{k-N_\mathrm{o}+2} & 0 & \cdots & 0 \\ \vdots & & \ddots & & \vdots \\ \boldsymbol{C}_{k-1}\left(\prod_{i=k-2}^{k-N_\mathrm{o}+1} A_i\right) & \boldsymbol{C}_{k-1}\left(\prod_{i=k-2}^{k-N_\mathrm{o}+2} A_i\right) & \cdots & \boldsymbol{C}_{k-1} & 0 \\ \boldsymbol{C}_{k}\left(\prod_{i=k-1}^{k-N_\mathrm{o}+1} A_i\right) & \boldsymbol{C}_{k}\left(\prod_{i=k-1}^{k-N_\mathrm{o}+2} A_i\right) & \cdots & \boldsymbol{C}_{k}\boldsymbol{A}_{k-1} & \boldsymbol{C}_{k} \end{bmatrix}}_{(N_\mathrm{o}p\times N_\mathrm{o}n)} \underbrace{\begin{bmatrix} \boldsymbol{\delta}_{\mathrm{x},k-N_\mathrm{o}} \\ \boldsymbol{\delta}_{\mathrm{x},k-N_\mathrm{o}+1} \\ \boldsymbol{\delta}_{\mathrm{x},k-N_\mathrm{o}+2} \\ \vdots \\ \boldsymbol{\delta}_{\mathrm{x},k-2} \\ \boldsymbol{\delta}_{\mathrm{x},k-1} \end{bmatrix}}_{(N_\mathrm{o}n\times 1)}
$$

$$
+ \underbrace{\begin{bmatrix} \boldsymbol{D}_{k-N_\mathrm{o}+1}\boldsymbol{u}_{k-N_\mathrm{o}+1} \\ \boldsymbol{D}_{k-N_\mathrm{o}+2}\boldsymbol{u}_{k-N_\mathrm{o}+2} \\ \boldsymbol{D}_{k-N_\mathrm{o}+3}\boldsymbol{u}_{k-N_\mathrm{o}+3} \\ \vdots \\ \boldsymbol{D}_{k-1}\boldsymbol{u}_{k-1} \\ \boldsymbol{D}_{k}\boldsymbol{u}_{k} \end{bmatrix}}_{(N_\mathrm{o}p\times 1)} + \underbrace{\begin{bmatrix} \boldsymbol{\delta}_{\mathrm{y},k-N_\mathrm{o}+1} \\ \boldsymbol{\delta}_{\mathrm{y},k-N_\mathrm{o}+2} \\ \boldsymbol{\delta}_{\mathrm{y},k-N_\mathrm{o}+3} \\ \vdots \\ \boldsymbol{\delta}_{\mathrm{y},k-1} \\ \boldsymbol{\delta}_{\mathrm{y},k} \end{bmatrix}}_{(N_\mathrm{o}p\times 1)} + \underbrace{\begin{bmatrix} \boldsymbol{v}_{k-N_\mathrm{o}+1} \\ \boldsymbol{v}_{k-N_\mathrm{o}+2} \\ \boldsymbol{v}_{k-N_\mathrm{o}+3} \\ \vdots \\ \boldsymbol{v}_{k-1} \\ \boldsymbol{v}_{k} \end{bmatrix}}_{(N_\mathrm{o}p\times 1)}
$$

The formulation of the measured outputs can be summarised in the following compact matrix notation

$$\boldsymbol{Y} = \boldsymbol{F}\boldsymbol{x}_{k-N_\mathrm{o}} + \boldsymbol{\Phi}_\mathrm{u}\boldsymbol{U} + \boldsymbol{\Phi}_\mathrm{w}\boldsymbol{W} + \boldsymbol{\Phi}_\mathrm{x}\boldsymbol{\Delta}_\mathrm{x} + \boldsymbol{\Phi}_\mathrm{d} + \boldsymbol{\Delta}_\mathrm{y} + \boldsymbol{V}. \tag{3.20}$$

With Equation (3.20) an expression for the discrepancy of the measured data to the estimated output is obtained depending on the variables to be optimised $\boldsymbol{x}_{k-N_\mathrm{o}}$ and $\{\boldsymbol{w}\}_{k-N_\mathrm{o}}^{k-1}$. This expression is substituted into the cost function Φ_k of the moving horizon observer's optimisation task (3.14)

$$\begin{aligned}
\Phi_\mathrm{k} &= \left(\boldsymbol{x}_{k-N_\mathrm{o}} - \hat{\boldsymbol{x}}_{k-N_\mathrm{o}|k-N_\mathrm{o}}\right)^T \boldsymbol{P}_{k-N_\mathrm{o}}^{-1} \left(\boldsymbol{x}_{k-N_\mathrm{o}} - \hat{\boldsymbol{x}}_{k-N_\mathrm{o}|k-N_\mathrm{o}}\right) + \boldsymbol{V}^T\boldsymbol{R}^{-1}\boldsymbol{V} + \boldsymbol{W}^T\boldsymbol{Q}^{-1}\boldsymbol{W} \\
&= \left(\boldsymbol{x}_{k-N_\mathrm{o}} - \hat{\boldsymbol{x}}_{k-N_\mathrm{o}|k-N_\mathrm{o}}\right)^T \boldsymbol{P}_{k-N_\mathrm{o}}^{-1} \left(\boldsymbol{x}_{k-N_\mathrm{o}} - \hat{\boldsymbol{x}}_{k-N_\mathrm{o}|k-N_\mathrm{o}}\right) \\
&\quad + \left(\boldsymbol{Y} - \boldsymbol{F}\boldsymbol{x}_{k-N_\mathrm{o}} - \boldsymbol{\Phi}_\mathrm{u}\boldsymbol{U} - \boldsymbol{\Phi}_\mathrm{w}\boldsymbol{W} - \boldsymbol{\Phi}_\mathrm{x}\boldsymbol{\Delta}_\mathrm{x} - \boldsymbol{\Phi}_\mathrm{d} - \boldsymbol{\Delta}_\mathrm{y}\right)^T \boldsymbol{R}^{-1} \\
&\quad \left(\boldsymbol{Y} - \boldsymbol{F}\boldsymbol{x}_{k-N_\mathrm{o}} - \boldsymbol{\Phi}_\mathrm{u}\boldsymbol{U} - \boldsymbol{\Phi}_\mathrm{w}\boldsymbol{W} - \boldsymbol{\Phi}_\mathrm{x}\boldsymbol{\Delta}_\mathrm{x} - \boldsymbol{\Phi}_\mathrm{d} - \boldsymbol{\Delta}_\mathrm{y}\right) + \boldsymbol{W}^T\boldsymbol{Q}^{-1}\boldsymbol{W}.
\end{aligned}$$

To make the derivation clearer, all known quantities are summarised in the vector $\boldsymbol{\Omega}$

$$\begin{aligned}
\boldsymbol{\Omega} &:= \underbrace{\boldsymbol{Y} - \boldsymbol{\Phi}_\mathrm{u}\boldsymbol{U} - \boldsymbol{\Phi}_\mathrm{d} - \boldsymbol{\Phi}_\mathrm{x}\boldsymbol{\Delta}_\mathrm{x} - \boldsymbol{\Delta}_\mathrm{y}}_{\text{known}} \\
\Phi_k &= \left(\boldsymbol{x}_{k-N_\mathrm{o}} - \hat{\boldsymbol{x}}_{k-N_\mathrm{o}|k-N_\mathrm{o}}\right)^T \boldsymbol{P}_{k-N_\mathrm{o}}^{-1} \left(\boldsymbol{x}_{k-N_\mathrm{o}} - \hat{\boldsymbol{x}}_{k-N_\mathrm{o}|k-N_\mathrm{o}}\right) \\
&\quad + \left(\boldsymbol{\Omega} - \boldsymbol{F}\boldsymbol{x}_{k-N_\mathrm{o}} - \boldsymbol{\Phi}_\mathrm{u}\boldsymbol{W}\right)^T \boldsymbol{R}^{-1} \left(\boldsymbol{\Omega} - \boldsymbol{F}\boldsymbol{x}_{k-N_\mathrm{o}} - \boldsymbol{\Phi}_\mathrm{u}\boldsymbol{W}\right) + \boldsymbol{W}^T\boldsymbol{Q}^{-1}\boldsymbol{W}.
\end{aligned}$$

In state estimation with the moving horizon state observer, the cost function Φ_k is minimised at each time step with respect to the optimisation variables $\boldsymbol{x}_{k-N_\mathrm{o}}$ and $\{\boldsymbol{w}\}_{k-N_\mathrm{o}}^{k-1}$. This solution of the optimisation task can be done with common quadratic solvers such as the Quadprog solver in Matlab®. For this reason, the minimisation task of the state estimation is restructured into the following quadratic form

$$\hat{\boldsymbol{x}}_{k|k} = \boldsymbol{f}\left(\hat{\boldsymbol{x}}_{k-N_\mathrm{o}|k}, \{\hat{\boldsymbol{w}}\}_{k-N_\mathrm{o}|k}^{k-1|k}\right) = \min_{\boldsymbol{x}_{k-N_\mathrm{o}}, \boldsymbol{W}} J =$$

$$\begin{aligned}
&\min_{\boldsymbol{x}_{k-N_\mathrm{o}}, \boldsymbol{W}} \quad 2 \cdot \begin{bmatrix} \boldsymbol{x}_{k-N_\mathrm{o}}^T & \boldsymbol{W}^T \end{bmatrix} \begin{bmatrix} \boldsymbol{P}_{k-N_\mathrm{o}}^{-1} + \boldsymbol{F}^T\boldsymbol{R}^{-1}\boldsymbol{F} & \boldsymbol{F}^T\boldsymbol{R}^{-1}\boldsymbol{\Phi}_\mathrm{w} \\ \boldsymbol{\Phi}_\mathrm{w}^T\boldsymbol{R}^{-1}\boldsymbol{F} & \boldsymbol{\Phi}_\mathrm{w}^T\boldsymbol{R}^{-1}\boldsymbol{\Phi}_\mathrm{w} + \boldsymbol{Q}^{-1} \end{bmatrix} \begin{bmatrix} \boldsymbol{x}_{k-N_\mathrm{o}} \\ \boldsymbol{W} \end{bmatrix} \\
&+ \begin{bmatrix} -\hat{\boldsymbol{x}}_{k-N_\mathrm{o}|k-N_\mathrm{o}}^T\boldsymbol{P}_{k-N_\mathrm{o}}^{-1} - \hat{\boldsymbol{x}}_{k-N_\mathrm{o}|k-N_\mathrm{o}}^T\boldsymbol{P}_{k-N_\mathrm{o}}^{-1\,T} - 2\boldsymbol{\Omega}^T\boldsymbol{R}^{-1}\boldsymbol{F} & -2\,\boldsymbol{\Omega}^T\boldsymbol{R}^{-1}\boldsymbol{\Phi}_\mathrm{w} \end{bmatrix} \begin{bmatrix} \boldsymbol{x}_{k-N_\mathrm{o}} \\ \boldsymbol{W} \end{bmatrix}
\end{aligned}$$

The generation of the linearised system matrices at a time k is always done by linearisation around the optimal estimated state $\hat{\boldsymbol{x}}_{k|k}$ at the current time. These system matrices $\boldsymbol{A}_k$, $\boldsymbol{B}_k$, $\boldsymbol{C}_k$, $\boldsymbol{D}_k$ and the offsets of the linearisation δ_x and δ_y are stored and used for this time step k, which is presented in Figure 3.1. Considering the horizon as a fixed window, the stored matrices are shifted backward by one time step after each state estimation until the horizon's end. The matrices are stored until they fall out of the window. Thus, at any given time k, those matrices are used for state estimation which are linearised around the estimated state $\hat{\boldsymbol{x}}_{k|k}$, based on the last $N_\mathrm{o}+1$ output measurements. The solution trajectory of the MHE $\hat{\boldsymbol{x}}$ consists of the estimates $\hat{\boldsymbol{x}}_{k|k}$ obtained from the local solution trajectory at each time step $\{\hat{\boldsymbol{x}}_{k-N_\mathrm{o}|k}, \hat{\boldsymbol{x}}_{k-N_\mathrm{o}+1|k}, \ldots, \hat{\boldsymbol{x}}_{k-1|k}, \hat{\boldsymbol{x}}_{k|k}\}$.
An alternative approach would be to linearise the system matrices at time k around the most recent solution trajectory $\{\hat{\boldsymbol{x}}_{k-N_\mathrm{o}|k}, \hat{\boldsymbol{x}}_{k-N_\mathrm{o}+1|k}, \ldots, \hat{\boldsymbol{x}}_{k-1|k}, \hat{\boldsymbol{x}}_{k|k}\}$. However, this would mean that the information of the output measurements $\{\boldsymbol{y}_{k-2\cdot N_\mathrm{o}}, \boldsymbol{y}_{k-2\cdot N_\mathrm{o}+1}, \ldots, \boldsymbol{y}_{k-N_\mathrm{o}-2}, \boldsymbol{y}_{k-N_\mathrm{o}-1}\}$ is not included in the horizon, since the system matrices are linearised around that solution which results from taking into account the output measurement $\{\boldsymbol{y}_{k-N_\mathrm{o}}, \boldsymbol{y}_{k-N_\mathrm{o}+1}, \ldots, y_{k-1}, y_k\}$. Therefore, the linearisation method presented is used in this work to capture as much information as possible in the observation horizon.
Through the linearisation around the own solution trajectory a certain error arises, which is investigated in more detail in Section 4.1.2.

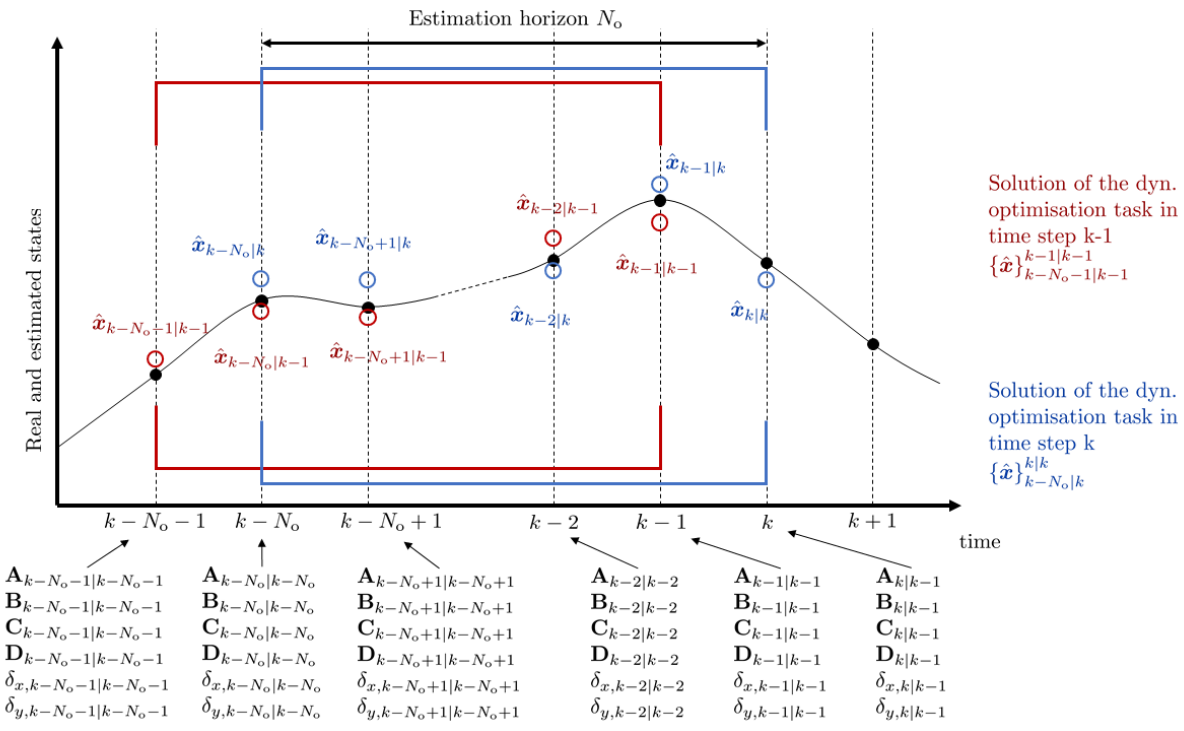

Figure 3.1: Concept for filling the horizon of the MHE with the linearised system matrices.

Chapter 4

Results and discussion

In the following chapter, the results of the moving horizon state estimation are presented and discussed and the observer is applied to two different systems. In the first step, the observer concept is applied to the FC model derived in Chapter 2, which represents a SISO system. To make further statements regarding possible applications in MIMO systems and the properties of the state estimator, the MHE concept is also validated on the nonlinear 3-tank system. The 3-tank system is characterised by its simplicity and numerical properties despite the two inputs and outputs and is therfore frequently used for research purposes.
The implementation and simulation are performed with Matlab. Output measurements and reference states are not taken from an experimental setup but are simulation based. First, the validation of the MHE concept on the fuel cell model is presented in this chapter. In addition, the effects of the perfect linearisation and the comparison with the EKF on the fuel cell model are introduced. In the second section, the validation of the MHE is carried out on the 3-tank model. Further properties of the observer, such as the basic validation of the MHE system matrices, effects of horizon length, and reconstruction of the initial state are investigated in more detail on the MIMO system.

4.1 PEM fuel cell system

4.1.1 MHE results

The moving horizon state estimation is tested on the fuel cell system for a standard operating cycle. In order to check the dynamic behaviour of the observer, different current steps are used as input signal. The simulations are performed starting from the operating point as defined in (2.75). This means, that no start-up or cold start of the fuel cell system is simulated. All simulations performed on the PEM fuel cell system are carried out with a sampling time of $T_s = 1\,\mathrm{ms}$.

At the beginning of the test run, the actual initial value $\boldsymbol{x}_0$ is passed to the observer as an inertial estimate $\hat{\boldsymbol{x}}_{0|0}$. The behaviour of the observer in the case of a deviating initial value or poor estimation $\hat{\boldsymbol{x}}_{0|0}$ is examined in detail in Section 4.2.3. First, the functionality of the state estimator is investigated under favourable conditions. Since the observer is given the actual state at the beginning of the simulation, the weighting matrix of the initial estimate $\boldsymbol{P}_0$ is also chosen to be correspondingly small. A low weighting in absolute numbers is equivalent to a small variance of the initial estimate $\hat{\boldsymbol{x}}_{0|0}$. The weighting matrix of the process noise $\boldsymbol{Q}$ and the measurement noise $\boldsymbol{R}$ are tuned for the specific model and set as follows

$$\boldsymbol{P}_0 = \begin{bmatrix} 10^{-10} & 0 & 0 & 0 & 0 \\ 0 & 10^{-10} & 0 & 0 & 0 \\ 0 & 0 & 10^{-10} & 0 & 0 \\ 0 & 0 & 0 & 10^{-10} & 0 \\ 0 & 0 & 0 & 0 & 10^{-3} \end{bmatrix},$$

$$\boldsymbol{Q} = \begin{bmatrix} 2 \cdot 10^{-11} & 0 & 0 & 0 & 0 \\ 0 & 2 \cdot 10^{-11} & 0 & 0 & 0 \\ 0 & 0 & 2 \cdot 10^{-13} & 0 & 0 \\ 0 & 0 & 0 & 2 \cdot 10^{-12} & 0 \\ 0 & 0 & 0 & 0 & 2 \cdot 10^{-5} \end{bmatrix}, \qquad \boldsymbol{R} = \begin{bmatrix} 5 \end{bmatrix}. \tag{4.1}$$

By choosing these three weighting matrices, which are also the tuning parameters of the observer, the behaviour and performance of the MHE can be specifically influenced. A rule of thumb for choosing the length of the observation horizon N_o is given by Rao and Rawlings [50], which states that the horizon should be chosen twice as large as the number of states of the system. In this implementation, a slightly larger horizon length of $N_\mathrm{o} = 15$ is chosen compared to the number of states, which is five. Furthermore, one should make sure that as many time constants of the system as possible can be mapped within the horizon. In the case of the fuel cell with a sampling time of 1 ms, however, it is not possible to cover all time constants in the horizon, as the largest is two seconds.

The measured outputs $\boldsymbol{y}$ and the actual states $\boldsymbol{x}$ do not come from an experiment but are generated by a simulation with the model from Chapter 2. To ensure that the observer's investigation is as close to reality as possible, both measurement and process noise are considered when generating the data.
The first state estimation is performed for the time index $k = 1$. If the state estimation is started, the horizon of the MHE must first be filled step by step with the output measurements and the system matrices belonging to this time step. For the time steps $k \leq N_\mathrm{o}+1$, all information available up to time k is used for the state estimation in each

case. Therefore, the optimisation task (3.11) is also referred to as the full information problem. Only from the time step $k > N_o + 1$ does the estimation on the receding horizon begin with the dynamic optimisation task (3.14).

This initialisation at the beginning of the simulation, where the equilibrium state is established, is not shown in Figure 4.1.
Figure 4.1 shows that the moving horizon estimator based on successive linearisation works on the highly nonlinear system of the fuel cell and estimates the states with satisfactory accuracy. Even with large changes in the input variable, the estimated states $\hat{\boldsymbol{x}}$ follow the actual states $\boldsymbol{x}$ without significant deviations. Furthermore, one can see that the moving horizon state estimation smoothes the states and does not precisely reproduce every noise signal. States like the mean membrane moisture λ_m, which have a significant influence on the output voltage V_{st}, are reproduced more accurately than other states. In the case of the estimated states in the cathode and anode, by contrast, one can see that these mainly rely on the model. Deviating behaviour is hardly estimated by the cathode and anode states or in a strongly damped form. Through the tuning parameters of the MHE, one can adjust the behaviour of the observer. If, for example, the process noise is weighted with higher values in $\boldsymbol{Q}$, the state estimator allows more significant deviations from the model.
Concerning the convergence behaviour, no issues or oscillating behaviour of the observer are detected. Even at the beginning of the simulation, when the horizon of the moving horizon estimator is not yet filled, the state estimator shows excellent convergence properties. Since the identical models are used in the creation of the reference data $\boldsymbol{y}$ and $\boldsymbol{x}$ and in the observer, this behaviour was basically to be expected. Nevertheless, this basic validation shows that the derived formulation of the MHE based on successive linearisation works well on the complex model of the fuel cell.

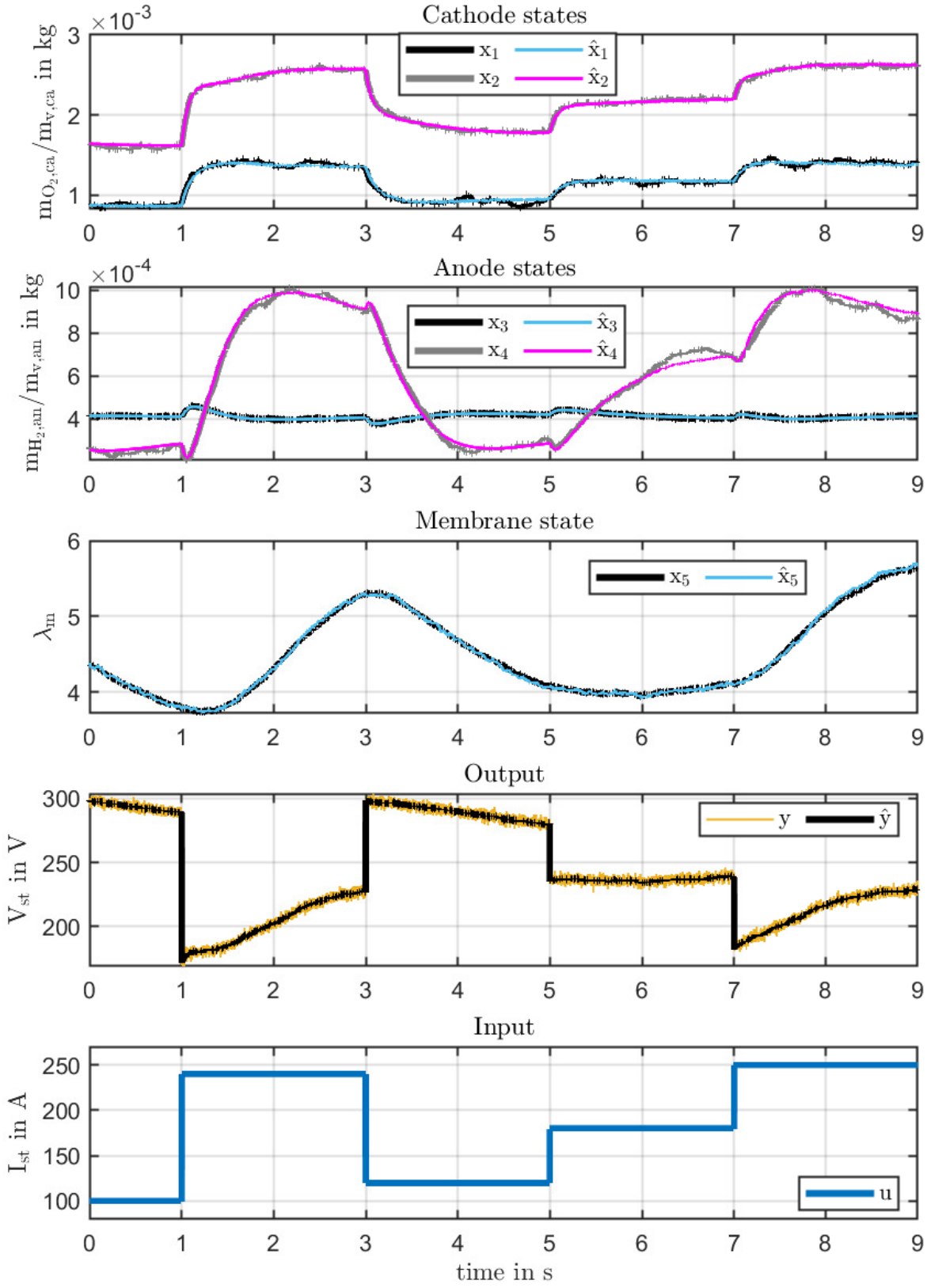

Figure 4.1: Results of the MHE with $N_o = 15$ on the PEMFC system

4.1.2 Effect of perfect linearisation

In this section, the effects of the inaccuracies arising from the linearisation of the system matrices are examined and compared with the results of the theoretically perfect linearisation.
The horizon of the MHE concept derived in Chapter 3 is filled with system matrices which are linearised around the solution trajectory $\hat{\boldsymbol{x}}$ generated by the MHE. Since the output data for the state observation is simulation based, the perfect theoretical solution $\boldsymbol{x}$ is known. The theoretically perfect solution $\boldsymbol{x}$ means those states which are generated by simulation of the model created in Chapter 2 under consideration of process and measurement noise.
Therefore, the presented MHE implementation is compared with the one where the horizon is filled with the theoretically perfect system matrices. The state estimation procedure of the perfect MHE is identical to the one presented in Chapter 3. The only difference between the presented MHE and the perfect MHE is that at the current time step k the system matrices are not linearised around the estimated state $\hat{\boldsymbol{x}}_{k|k}$ but around the theoretically perfect solution $\boldsymbol{x}_k$ obtained from the reference model.
All results of the theoretically perfect MHE concept are given the index "perfect", such as the estimated states $\hat{\boldsymbol{x}}_{\text{perfect}}$.

This comparison is carried out on the PEMFC system. All simulation settings, as well as weighting matrices, initial estimate $\hat{\boldsymbol{x}}_{0|0}$ and output data of the simulation ($\boldsymbol{y}$, $\boldsymbol{x}$ and $\boldsymbol{u}$), are chosen similar to Section 4.1.1 and are equal for both MHEs. In the Table 4.1 corresponds $\hat{\boldsymbol{x}}$ to the results of the presented MHE. The relative estimation error related to the theoretically perfect solution $\boldsymbol{x}$ was used in Table 4.1 as a criterion to compare the results of the MHE and the perfect MHE.

Horizon length N_o	$\frac{\lvert\boldsymbol{x}-\hat{\boldsymbol{x}}\rvert}{\lvert\boldsymbol{x}\rvert}\cdot\%$	$\frac{\lvert\boldsymbol{x}-\hat{\boldsymbol{x}}_{\textbf{pefect}}\rvert}{\lvert\boldsymbol{x}\rvert}\cdot\%$
$N_\text{o}=1$	1.3047	1.2861
$N_\text{o}=5$	1.2920	1.2867
$N_\text{o}=10$	1.2913	1.2882
$N_\text{o}=20$	1.2910	1.2898
$N_\text{o}=30$	1.2909	1.2911

Table 4.1: Effects of horizon length on the estimation result

The quantitative comparison in Table 4.1 shows that the influence of the linearisation error on the performance of the observer decreases with increasing horizon length. For a horizon length of $N_\text{o}=5$ or higher, there is hardly any difference in the performance of

the two estimation results. This investigation is a purely theoretical analysis in which the reference states $\boldsymbol{x}$ are generated with the same model as used in the MHE. In real applications, a more significant discrepancy between the model in the observer and the actual model of the system is to be expected and therefore, deviations such as those between the MHE and the perfect MHE can therefore be neglected. It can be concluded, that the formulation of the MHE derived in Chapter 3 has sufficient accuracy.

4.1.3 Comparison of MHE and EKF

In the following, the moving horizon estimator is compared with the extended Kalman filter, which is characterised by a significantly lower computing time and more straightforward implementation. The fundamental relation between the MHE with horizon length one and the EKF is presented in [43].
The comparison is made with an EKF formulation, which is also based on successive linearisation [11]. In this formulation, the required Jacobians are generated by analytically deriving the system equations and the linearisation offsets are included in the observer equations as well.
The comparison of the two types of observers is carried out on the PEMFC model. In order to make statements about possible differences between the two state estimators, both receive the same weighting matrices. As with the MHE, the EKF weights the initial estimate with $\boldsymbol{P}_0$, the process disturbances with $\boldsymbol{Q}$ and the measurement noise with $\boldsymbol{R}$. If the MHE and the EKF receive the same weighting matrices, it is ensured that both observer concepts have equal confidence in the model, respectively, the output measurements. These weighting matrices are the same as in Section 4.1. Other simulation parameters, such as the initial values for $\boldsymbol{y}$ and $\boldsymbol{x}$ also remained unchanged. In this investigation, an alternative input signal $\boldsymbol{u}$ is used compared to Section 4.1.1. At the beginning of the simulation, the state estimators receive the actual initial value $\boldsymbol{x}_0$ as an initial estimate $\hat{\boldsymbol{x}}_{0|0}$. The observation horizon of the moving horizon observer in this case is set to $N_\mathrm{o} = 15$ again.

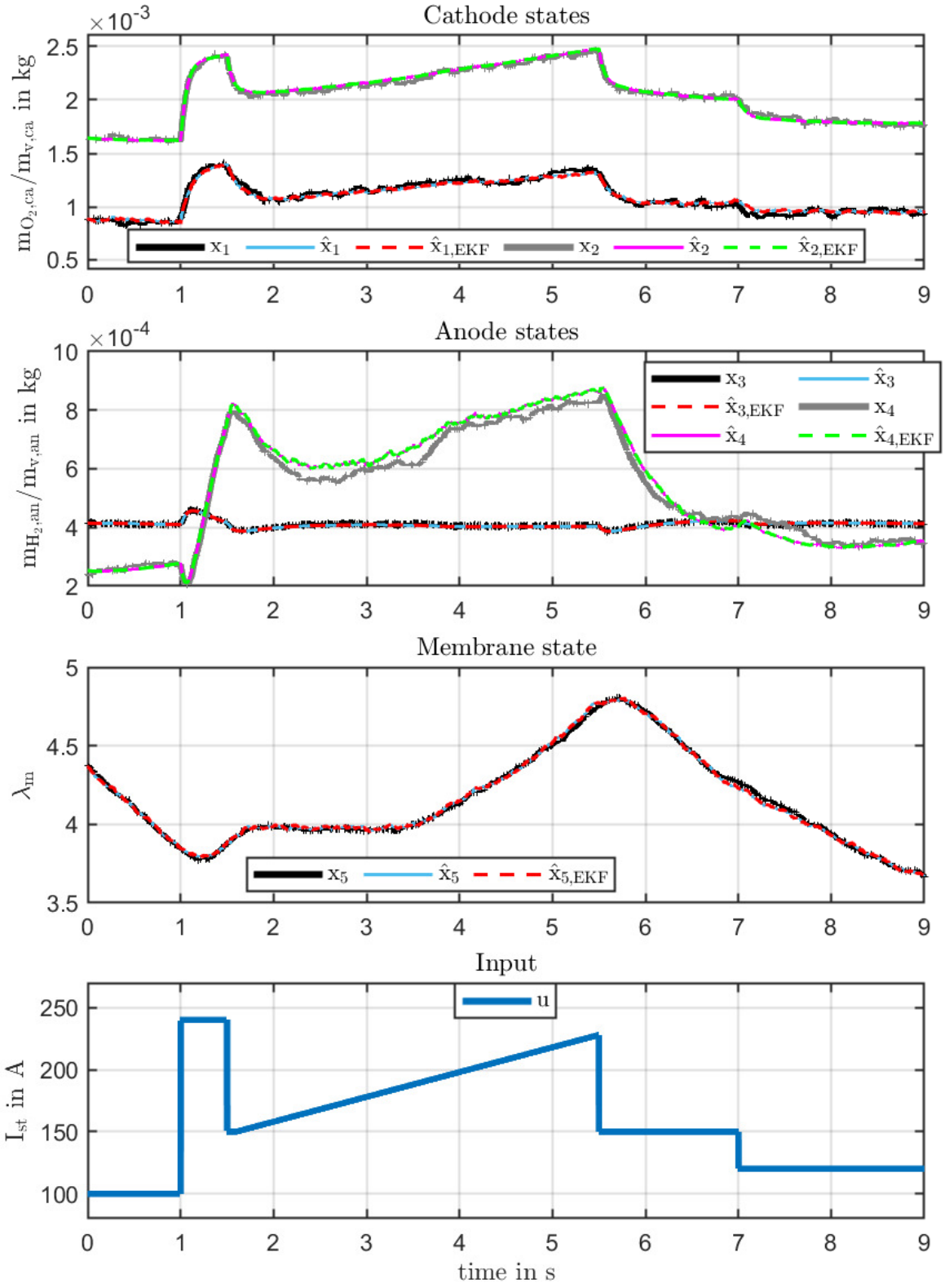

Figure 4.2: Comparison of MHE with $N_o = 15$ and EKF, both observers based on successive linearisation

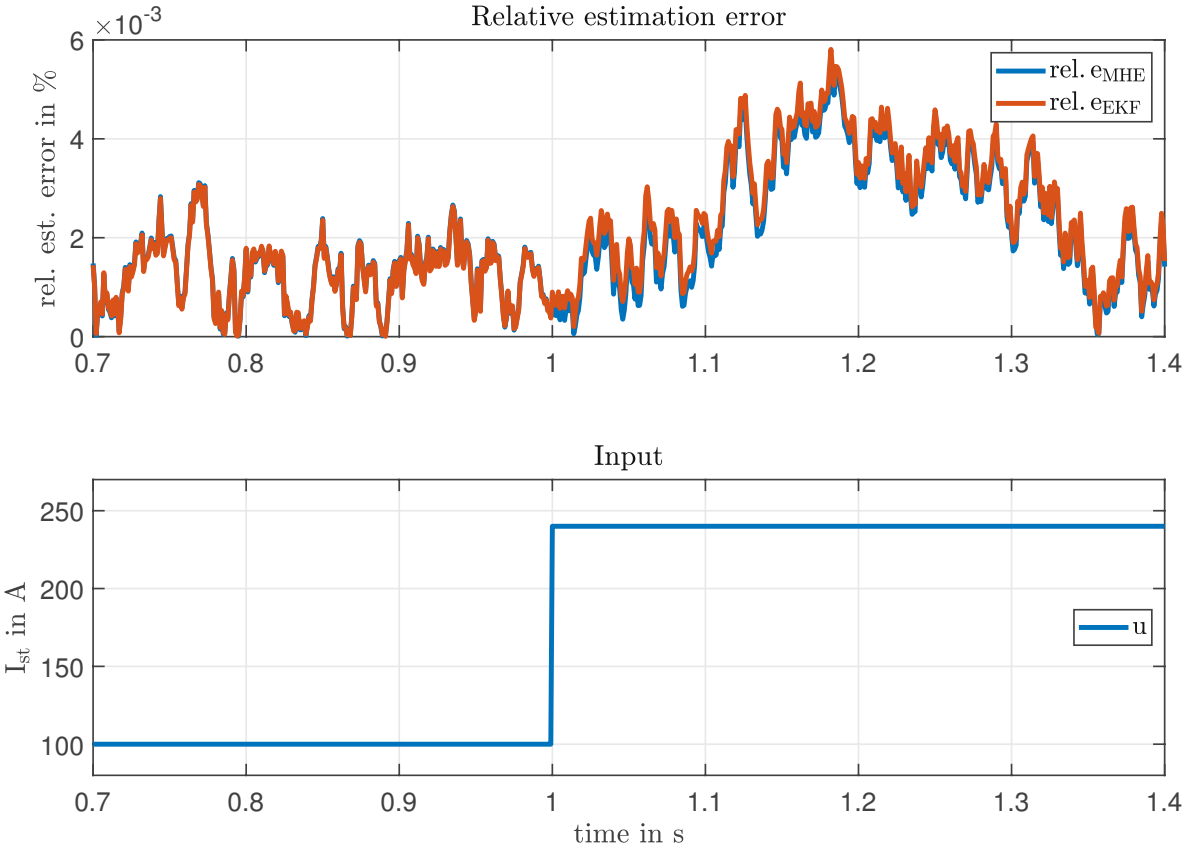

Figure 4.3: Evolution of the relative estimation error of MHE with $N_o = 15$ and EKF in the case if a sudden change of the stack current I_{st}

The comparison of the time signals of the state estimation is shown in Figure 4.2. Visually, no qualitative difference between the two observer concepts can be detected. This statement is also confirmed by Table 4.2, where the relative estimation errors of the estimation results are compared. The relative estimation error refers in each case to the reference states $\boldsymbol{x}$.

	rel. error in %
MHE wih $N_o = 15$	1.7165
EKF	1.7256

Table 4.2: Comparison of the relative estimation error of the MHE with $N_o = 15$ and the EKF

The time signals and the quantitative comparison of the error show hardly any differences in the performance and dynamic behaviour for both observers. The advantage

of including past output measurements in the state estimation is only evident in the behaviour on abrupt changes in the input variable. As shown in Figure 4.3 in the course of the relative estimation error, the MHE reacts minimally better to steps in the input variable $\boldsymbol{u}$. In steady-state, both observers follow precisely the same solution trajectory.

A similar comparison between the moving horizon estimator and the extended Kalman filter is made in [51]. This work shows the differences in the convergence behaviour of the two observer concepts. The EKF converges to a false solution or diverges if multiple states satisfy the steady-state measurements, or the observer is given a poor estimate of the initial state. The MHE, on the other hand, shows excellent convergence properties in these two cases. For the variant of the MHE presented in this thesis, however, it should be noted that these statements are not generally valid. An essential condition for the MHE based on successive linearisation is that the system can also be linearised at critical points, which may lead to singular system matrices.

The previous investigations in this chapter have shown that the MHE based on successive linearisation runs on the highly nonlinear model of the fuel cell and estimates the states with sufficient accuracy. However, statements on the general applicability to nonlinear MIMO systems cannot be made since the model of the fuel cell from Chapter 2 is a SISO system. Furthermore, it should be mentioned again that some of the time constants of the fuel cell are too large to capture them in the observation horizon since the computational effort increases strongly with long observation horizons. For this reason, the validation of the MHE concept in the next section is performed on the nonlinear 3-tank system, which represents a MIMO system.

4.2 3-tank system

The 3-tank is a nonlinear system with two inputs and two outputs in the considered configuration and is described by three states. Figure 4.4 shows the schematic configuration of the system.
The water levels h_1, h_2 and h_3 of the three containers, which have the same diameter, represent the three states of the system. On the one hand, water can enter the tanks through the two inputs mass flows $\dot{V}_{\text{in},1}$ and $\dot{V}_{\text{in},2}$, which also represent the inputs of the system u_1 and u_2. On the other hand, water can get into and out of the tanks through the outflows or connections between the tanks. How large these outflows and mass flows between the tanks are depends on the respective filling levels in the tanks. This relations gives the 3-tank system its nonlinear characteristic.
The goal is to estimate the development of the states based on the two output measurements $y_1 = h_1$ and $y_2 = h_3$. These two output measurements are subject to uncertainty and measurement noise.

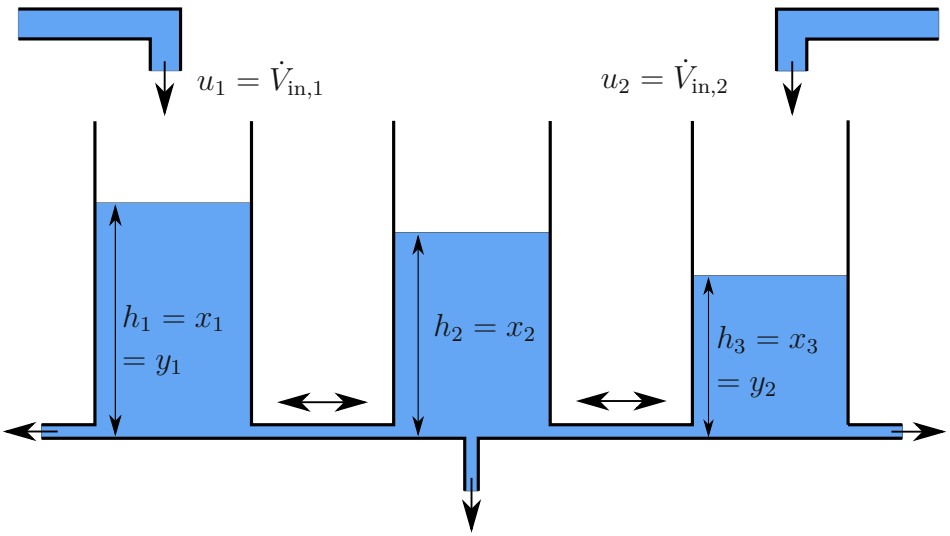

Figure 4.4: Schematic illustration of the 3-tank system

The time constants of the system range from 13 to 120 seconds. Therefore, a sampling time of $T_\text{s} = 2\,\text{s}$ is chosen for all simulations with the 3-tank system.
As with the fuel cell system, the measured outputs and the states to be observed of the 3-tank system do not originate from measurements of an experimental setup but were generated by a simulation with the corresponding noise signals in Matlab. When generating the output data, noise signals are added to both the system and the output

equation to represent the process or measurement noise. The model parameters are also changed by a few percent when generating $\boldsymbol{y}$ and $\boldsymbol{x}$. This measure is intended to get a slight deviation between the model in the simulation and the model of the MHE to challenge the observer.

MHE results

In this section, the MHE concept derived in Chapter 2 is validated on the nonlinear 3-tank syste, where the horizon length can be chosen to capture all time constants of the system with acceptable computational effort.

The length of the observation horizon is set to $N_\mathrm{o} = 70$ to capture all time constants of the system. The weighting matrices $\boldsymbol{P}_0$, $\boldsymbol{Q}$ and $\boldsymbol{R}$, which represent the tuning parameters of the observer in addition to the horizon length N_o, represent the covariance matrices of the initial estimation and the noise signals. The following weights are chosen for the validation of the MHE

$$\boldsymbol{P}_0 = \begin{bmatrix} 1 & 0 & 0 \\ 0 & 1 & 0 \\ 0 & 0 & 1 \end{bmatrix}, \qquad \boldsymbol{Q} = \begin{bmatrix} 0.05 & 0 & 0 \\ 0 & 0.05 & 0 \\ 0 & 0 & 0.05 \end{bmatrix}, \qquad \boldsymbol{R} = \begin{bmatrix} 6 & 0 \\ 0 & 6 \end{bmatrix}. \tag{4.2}$$

The results of the state estimation with these settings are illustrated in Figure 4.5. On the 3-tank system, a satisfactory accuracy could be achieved with the moving horizon state estimation concept based on successive linearisation, especially for the non-measurable state h_2. One can observe smoothing effects of the MHE at the states, similar to the fuel cell. No significant deviations of the estimated state trajectory can be detected with this nonlinear MIMO system, as is the case for the fuel cell model, even with abrupt input variable changes. As with the fuel cell, it was to be expected that the MHE converges fast since almost the same model is used in the MHE and in generating the initial data $\boldsymbol{y}$ and $\boldsymbol{x}$. The estimated states in Figure 4.5 show that the MHE based on successive linearisation also works on the MIMO system and estimates the non-measurable states without significant deviation.

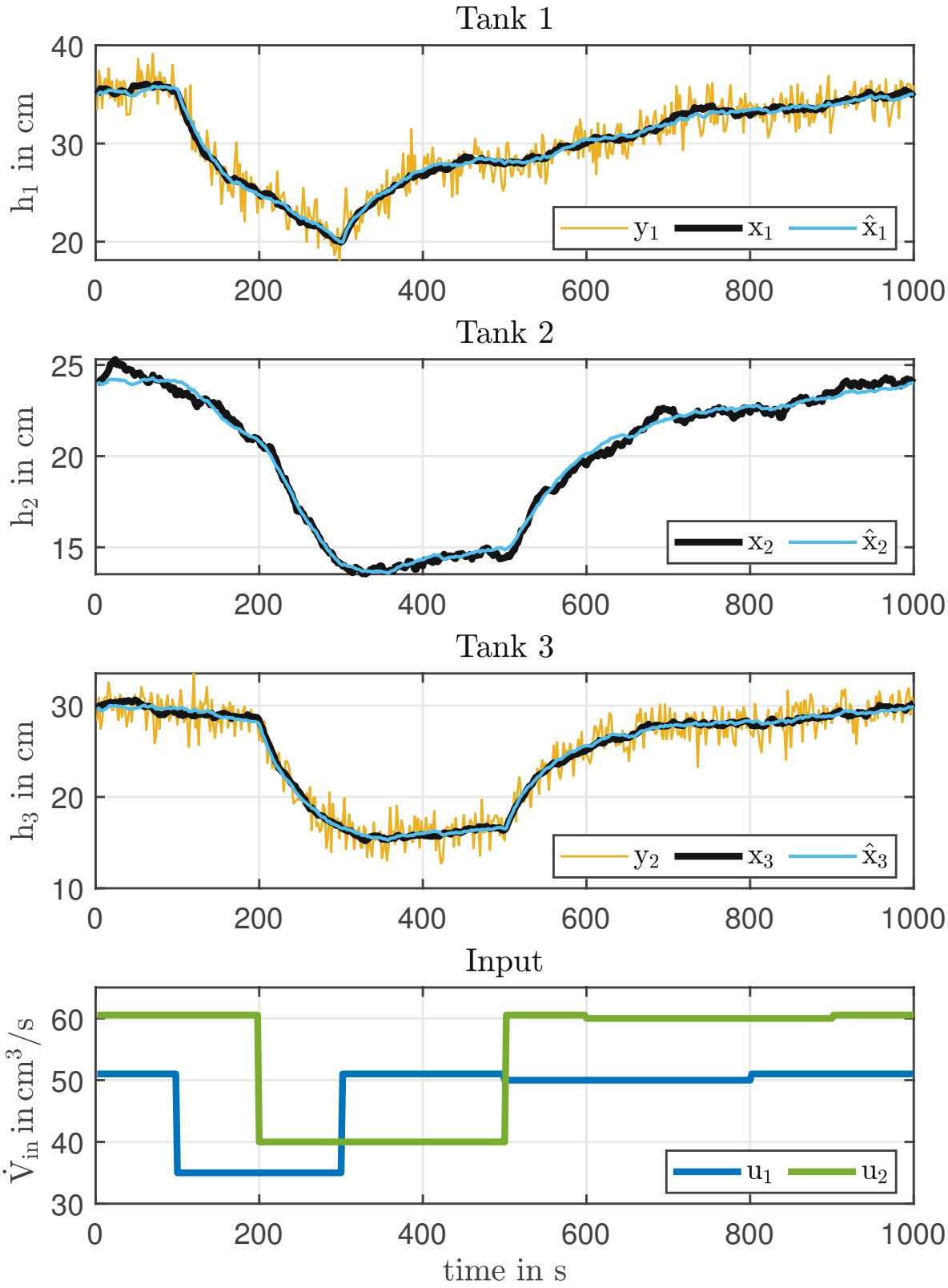

Figure 4.5: Results of the MHE with $N_o = 70$ on the nonlinear 3-tank system

4.2.1 Validation of the MHE system matrices

For a state estimator to work generally on a real system with modelling inaccuracies, process and measurement noise, a fundamental requirement is that the observer can reproduce the model numerically accurately in the undisturbed case. In this section, this accuracy of the observer is checked. Ideally, the MHE should reproduce the system numerically exactly so that the state estimator does not need to make any correction. As a reference, the nonlinear 3-tank model is simulated over time based on the standard ODE45 Solver of Matlab, which is based on the Runge-Kutta method. When simulating the system with ODE45, no process and measurement noise are taken into account, because this validation only concerns the model itself.

To check the accuracy of the formulation of the MHE derived in Chapter 3.14, all weighting matrices are chosen as unit matrices and the true state $\boldsymbol{x}_0$ is passed to the observer as an initial estimate $\hat{\boldsymbol{x}}_{0|0}$. A horizon length $N_\mathrm{o} = 70$ is chosen when estimating the states with the MHE. As with the previous analysis, a sampling time of two seconds is selected.

Figure 4.6 shows the comparison of the two results of the simulation with the ODE45 method and the estimation with the MHE. It can be seen that the moving horizon observer can reproduce the model with the same accuracy. Even with abrupt changes of the states, the solution trajectory of the MHE does not deviate from the result simulated in Matlab, which means that the solution proved by the MHE is the exact solution of the undisturbed model itself.
This basic validation proves that the formulation of the MHE concept derived in Chapter 3.14 has sufficient accuracy for nonlinear MIMO systems.

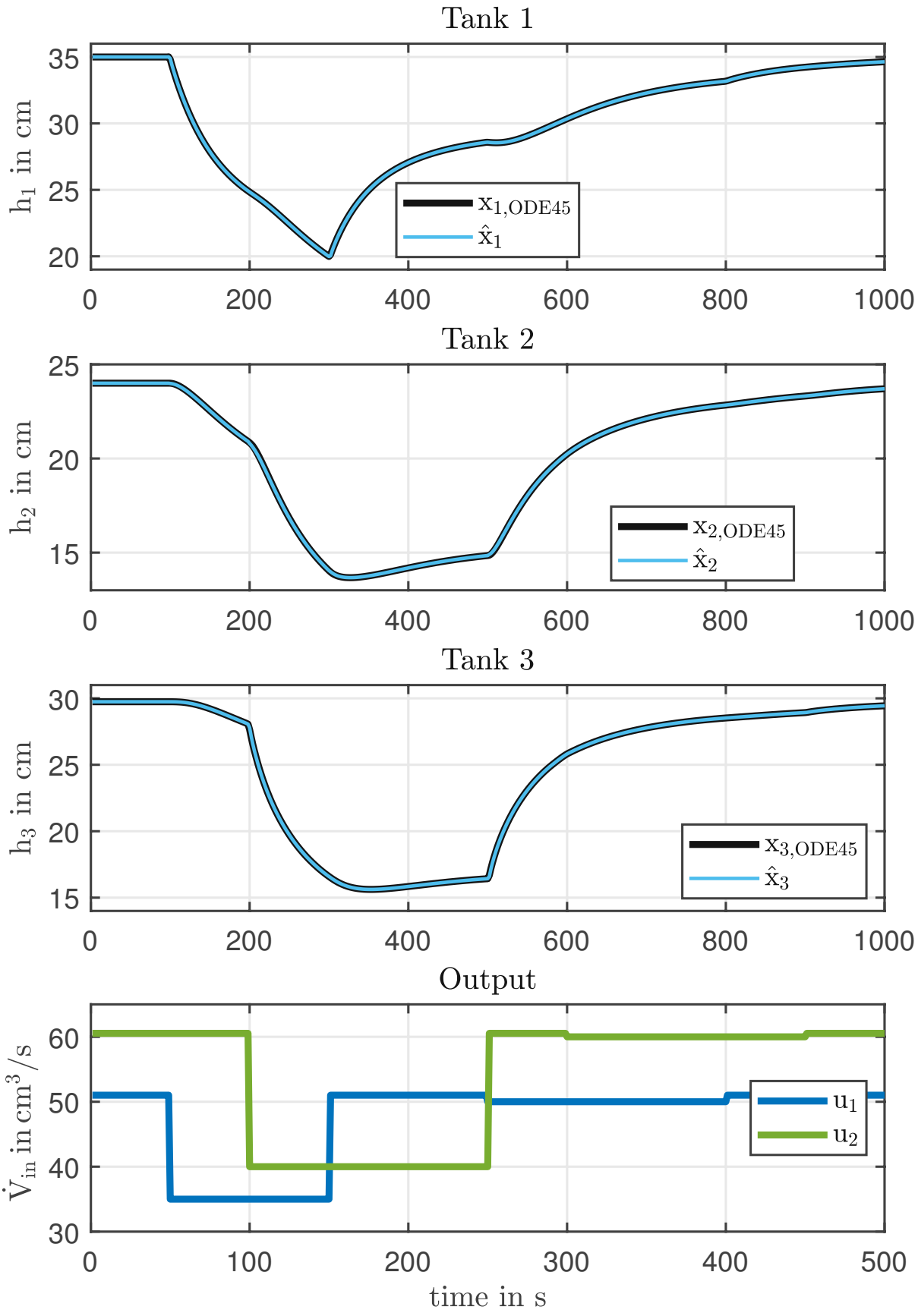

Figure 4.6: Comparison of MHE with $N_o = 70$ for simulation purposes to the model simulated with ODE45

4.2.2 Effects of horizon length

One problem of the MHE on the fuel cell system is that not all time constants can be captured within a manageable horizon. On the 3-tank system this is possible because the time constants are in the range of 13 to 120 seconds. This section therefore investigates the effect of the horizon length on the observer's performance.
From a probabilistic point of view, the result of the MHE should converge to the actual state of the system as the horizon length increases. If one extends the observation horizon to the extreme case $N_o = 1 : k$, one obtains optimal estimation result in theory.

For comparison of the MHE with different horizon lengths, the exact same simulation parameters and weighting matrices are used as in Section 4.2. To be able to compare the results, the same initial data $\boldsymbol{y}$, $\boldsymbol{x}$ and $\boldsymbol{u}$ are used in each run. As in the simulation in Section 4.2, the actual state $\boldsymbol{x}$ is passed to the MHE as an initial estimate $\hat{\boldsymbol{x}}_{0|0}$.
Table 4.3 shows the quantitative comparison of the moving horizon estimator results with different horizon lengths N_o on the 3-tank system. The performance of the state estimation is evaluated in each case with the relative estimation error related to the reference state $\boldsymbol{x}$.

Horizon length N_o	$\frac{\lvert\boldsymbol{x}-\hat{\boldsymbol{x}}\rvert}{\lvert\boldsymbol{x}\rvert} \cdot \%$
$N_o = 1$	1.0982
$N_o = 10$	1.0980
$N_o = 50$	1.0981
$N_o = 100$	1.0981
$N_o = 150$	1.0981

Table 4.3: Effects of horizon length N_o on the estimation accuracy

The results in Table 4.3 show that there is only a minimal improvement in the estimation results with increasing horizon length. Moreover, even for horizon lengths where the information can be obtained for all time constants, there is no significant improvement in the estimation accuracy. One explanation is that linearisation produces a certain error, which accumulates with increasing horizon length and thus reduces the advantages of the larger optimisation horizon.

4.2.3 Reconstruction of initial states

In some technical applications, such as estimating the battery state of charge, not only the knowledge of the current state of the system is important, but also the reconstruction of the initial state $\boldsymbol{x}_0$. The moving horizon observer is suitable for such applications since it estimates the states at the beginning of the horizon at every time step. In this section, this property is investigated in detail. For this reason, the observer is given an initial value $\hat{\boldsymbol{x}}_{0|0}$, which differs from the actual initial state $\boldsymbol{x}_0$.
To assess the behaviour of the observer and exclude the influence of the noise signals, the simulation is carried out without interfering signals. This means that no process or measurement noise is considered when generating the output measurements $\boldsymbol{y}$, and the reference states $\boldsymbol{x}$.

The results of the reconstruction of the initial state on the 3-tank system are illustrated in Figure 4.7. In this figure, $\hat{\boldsymbol{x}}$ is the solution trajectory of the MHE, which represents the estimated solution at each time step k based on the initial measurements $\{\boldsymbol{y}_0, \boldsymbol{y}_1, \dots \boldsymbol{y}_{k-1}, \boldsymbol{y}_k\}$. The solution trajectory of the full information optimisation problem at time step j is given by $\{\hat{\boldsymbol{x}}\}_{0|j}^{j|j}$, which is equal to $\{\hat{\boldsymbol{x}}_{0|j}, \hat{\boldsymbol{x}}_{1|j} \dots \hat{\boldsymbol{x}}_{j-1|j}, \hat{\boldsymbol{x}}_{j|j}\}$. The same notation is used here as in the probabilistic derivation in Section 3.2. The estimate of the state $\boldsymbol{x}_i$ at time j obtained from the optimisation task (3.11) is $\hat{\boldsymbol{x}}_{i|j}$.
The weighting matrices of the process and measurement noise $\boldsymbol{Q}$ and $\boldsymbol{R}$ are chosen the same as in Section 4.2. This analysis focuses on the reconstruction of the initial state and not on the performance of the observer. Therefore, the following modified weighting matrix $\boldsymbol{P}_0$ is used in this investigation

$$\boldsymbol{P}_0 = \begin{bmatrix} 20 & 0 & 0 \\ 0 & 40 & 0 \\ 0 & 0 & 20 \end{bmatrix}. \tag{4.3}$$

Figure 4.7 shows that the MHE can reconstruct the states and especially the non-measurable state h_2 after a few sampling intervals with good accuracy. The measurable states h_1 and h_3 can already be estimated correctly after a few time steps, as was expected. Depending on the choice of weights, the MHE can be optimised both in terms of performance and fast reconstruction of the initial state.

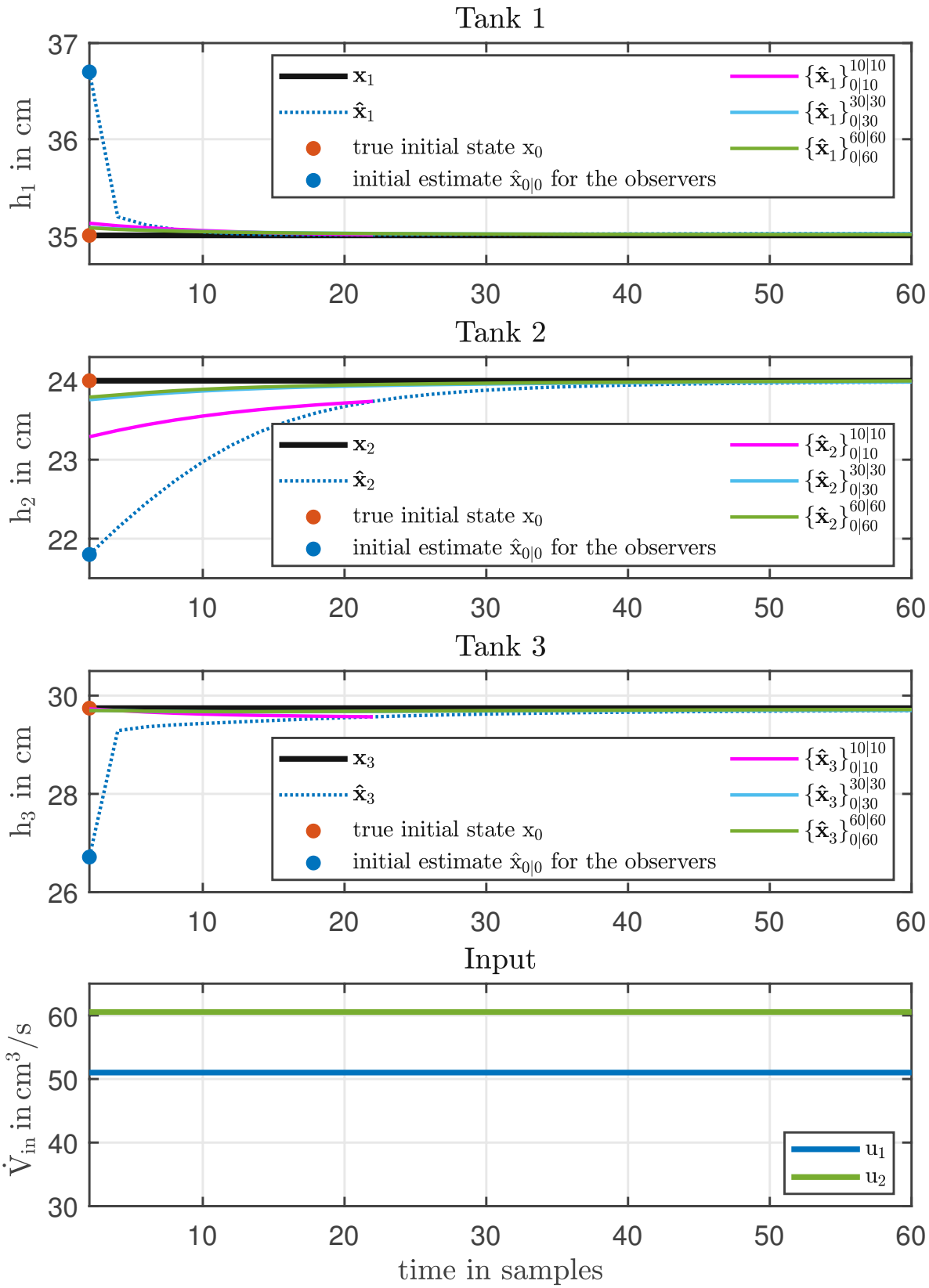

Figure 4.7: Reconstruction of the initial state $\boldsymbol{x}_0$ on the 3-tank system for different horizon lengths

Chapter 5

Conclusion

Due to the growing demand for sustainable and environmentally friendly alternative energy sources, the fuel cell has moved into the focus of scientific interest in recent years. A significant challenge is to ensure the stable and efficient operation of the fuel cell. In order to achieve this objective, the relevant internal states, which in most cases cannot be measured, must be observed. The reconstruction of states based on output measurements is done with such observers. Thus, for this important instrument in engineering, the proper method and an appropriate system model have to be available and analysed to guarantee reliable monitoring of the states.

To reach real-time state estimation, it is essential to find a mathematical representation of a system that offers a good compromise between accuracy and computational effort. Zero-dimensional system models are chosen thesis to achieve this goal. As with many other PEMFC models in literature, the model introduced in Chapter 2 is based on the work of Pukrushpan [6]. Fundamental effects such as transient effects of mass flow in the cathode and anode, electroosmotic drag, back diffusion and voltage losses due to ohmic resistance, activation losses and concentration losses are considered in this model. To obtain a generally valid fuel cell model, some empirical calculation formulas are replaced by basic equations. To represent the fundamental relationship between the input current I_{st} and the output voltage U_{st}, the model was additionally extended with the effect of transient rewetting of the membrane, as in [9]. Although the PEMFC model is not parametrised to a specific fuel cell stack, the basic system behaviour matches with the simulation results of [6] and thus represents an interesting model for testing the nonlinear state estimation method.

In the presented formulation of the MHE concept derived in Chapter 3, the focus is on a straightforward matrix based and low-computation implementation. To meet these requirements, the nonlinear system is linearised in each time step. The particularly

high accuracy is achieved by considering the linearisation offsets as well. Through the implementation based on successive linearisation, a compact matrix structure is derived for the dynamic optimisation task of the MHE, which can be solved in each time step with common quadratic solvers.

The first validation of the state estimation method was done on the nonlinear system of the fuel cell. The simulation results in Section 4.1.1 show that the moving horizon observer based on successive linearisation estimates the states for the complex system with satisfactory accuracy. A positive feature of the moving horizon estimator is that the states are not only well estimated but also smoothed at the same time. This means that the estimated state can be passed on to the controller for calculation of the control variable without further filtering. Furthermore, no behaviour indicating poor convergence could be conducted neither at the beginning of the simulation nor for input steps.

The investigations on the fuel cell in Section 4.1.2 show that there is only a minimal improvement in the performance of the MHE if the system matrices in the observer's horizon are generated around a theoretically perfect solution $\boldsymbol{x}$ instead of linearising around the solution trajectory of the MHE. The implication is that the formulation of the MHE derived in Chapter 3 has sufficient accuracy.

Comparing MHE and EKF on the PEMFC system, minimal differences in the performance of the two observers could be detected. In steady-state, both state estimators follow the same solution trajectory. Only in the case of abrupt changes in the input variables slight differences in the simulation in Section 4.1.3 are detected in favour of the MHE. However, there are differences in the convergence properties. In the case of a poor inertial estimate or if there are several states of the system satisfying measurements, the EKF in many instances does not converge or converges against the wrong solution [51]. In the EKF, the state distribution is approximated by a Gaussian random variable, which is then propagated through the linearised system. This assumption can result in deviations from the true posterior mean and variance, which in the worst case can lead to a divergence of the EKF [52]. Although the same assumptions are made in the arrival cost term of the MHE, these deviations do not affect convergence as much due to the longer observation horizon.
Other advantages of the moving horizon state estimation are that the assumption of Gaussian noise signals does not have to be fulfilled for the implementation of the MHE [17]. Furthermore, the generated and stored system matrices can be used for the control concept.

In the second part of Chapter 4, the observer concept is validated on the nonlinear

3-tank system. Compared to the fuel cell model, the poles of the 3-tank are close together and thus the MHE can capture all time constants of the system with an appropriate horizon length. The results in Section 4.2 show that the MHE based on successive linearisation estimates the states of the multivariable 3-tank without significant deviations. The non-measurable fill level of the three tanks are also observed with satisfactory accuracy. Although a discrepancy between the observer's model and the one used when generating the reference data is created by slight parameter variation, the MHE converges towards the true state from the beginning of the simulation.

According to the probabilistic interpretation in Section 3.2, the result of the MHE should be converging to the actual states as the horizon length increases. However, the investigations on the 3-tank system in this thesis show that the horizon length has only a minimal influence on the performance of the moving horizon state estimation. Even for horizon lengths where all time constants of the system are captured, no significant improvements in the estimation result are observed. One explanation for this is that due to the stepwise linearisation of the system, the linearisation errors add up with increasing horizon length and thus cancel out the positive effects of a longer observation horizon.

Another possible application of the MHE is shown in Section 4.2.3 for the 3-tank system. An alternative weighting of the initial estimate $\boldsymbol{P}_0$ decisively influences the convergence behaviour of the observer in this analysis. If the moving horizon observer receives a poor initial estimate, the reconstruction of the initial state is done within a few sampling intervals with sufficient accuracy. This property can be helpful in technical applications, such as estimating the state of charge of a battery. Thus, it can be concluded that the MHE can be optimised and driven in terms of performance as well as convergence.

The further development of this moving horizon state estimation concept can be done by an alternative formulation of the arrival costs. The arrival costs are a fundamental element of the MHE as they summarise data not contained in the horizon. In this work, the arrival costs are calculated based on the assumption that the conditional probability density function of the state at the beginning of the horizon approximates based on a normal distribution. Nonlinearities of the system and constraints can cause this distribution to become non-Gaussian, introducing an error in the arrival cost term. This error can be compensated by extending the observation horizon. However, this measure would lead to a significantly higher computation time and thus hamper the implementation of online applications. Sample-based approaches such as the particle filter [53] could be used to estimate the parameters of the arrival costs. With the help of this filter method, which is based on the Monte Carlo method, a non-Gaussian prob-

ability density function can also be approximated. The more accurate approximation of the data not included in the horizon can increase the state estimation quality.
Furthermore, state estimation could be extended by constraints on the states or noise signals. Model errors can be compensated for by constraining the states, or model simplification can be achieved. However, care must be taken when constraining the states. Unlike a controller, a state estimator cannot enforce compliance with bounds in the real system. A wrong choice of bounds can therefore lead to unphysical acausalities [17]. On the other hand, the observer can also estimate states that represent a solution to the optimisation task but are not physically possible, such as negative masses. Therefore, constraints are probably necessary for implementation.

Bibliography

[1] Ryan O'hayre, Suk-Won Cha, Whitney Colella, and Fritz B Prinz. *Fuel cell fundamentals*. John Wiley & Sons, 2016.

[2] co2online. Funktionsweise der brennstoffzelle. `https://www.co2online.de/modernisieren-und-bauen/brennstoffzellen-heizung/was-sind-brennstoffzellen/`. Accessed: 2021-08-17.

[3] European Commission. 2050 long-term strategy. `https://ec.europa.eu/clima/policies/strategies/2050_de`. Accessed: 2021-08-16.

[4] Stadt Wien. Der wiener klimapakt. `https://www.wien.gv.at/regierungsabkommen2020/lebenswerte-klimamuster-stadt/der-wiener-klimapakt/`. Accessed: 2021-08-16.

[5] Bosch. the mobility of the future needs fuel cells. `https://www.bosch-presse.de/pressportal/de/en/bosch-die-mobilitaet-der-zukunft-braucht-die-brennstoffzelle-218112.html`. Accessed: 2021-08-16.

[6] Jay Tawee Pukrushpan. *Modeling and control of fuel cell systems and fuel processors*. PhD thesis, University of Michigan Ann Arbor, Michigan, USA, 2003.

[7] Ling Hong, Jian Chen, Zhiyang Liu, Lianghui Huang, and Zhongle Wu. A nonlinear control strategy for fuel delivery in pem fuel cells considering nitrogen permeation. *International Journal of Hydrogen Energy*, 42(2):1565–1576, 2017.

[8] Liangfei Xu, Junming Hu, Siliang Cheng, Chuan Fang, Jianqiu Li, Minggao Ouyang, and Werner Lehnert. Robust control of internal states in a polymer electrolyte membrane fuel cell air-feed system by considering actuator properties. *International journal of hydrogen energy*, 42(18):13171–13191, 2017.

[9] Daniel Ritzberger, Christoph Hametner, and Stefan Jakubek. A real-time dynamic fuel cell system simulation for model-based diagnostics and control: Validation on real driving data. *Energies*, 13(12):3148, 2020.

[10] Dominik Murschenhofer, Dominik Kuzdas, Stefan Braun, and Stefan Jakubek. A real-time capable quasi-2d proton exchange membrane fuel cell model. *Energy conversion and management*, 162:159–175, 2018.

[11] Lukas Böhler, Daniel Ritzberger, Christoph Hametner, and Stefan Jakubek. Constrained extended kalman filter design and application for on-line state estimation of high-order polymer electrolyte membrane fuel cell systems. *international journal of hydrogen energy*, 46(35):18604–18614, 2021.

[12] Kui Chen, Salah Laghrouche, and Abdesslem Djerdir. Fuel cell health prognosis using unscented kalman filter: Postal fuel cell electric vehicles case study. *International Journal of Hydrogen Energy*, 44(3):1930–1939, 2019.

[13] Martin Schultze and Joachim Horn. State estimation for pem fuel cell systems with time delay by an unscented kalman filter and predictor strategy. In *21st Mediterranean Conference on Control and Automation*, pages 104–112. IEEE, 2013.

[14] Maxime Piffard, Mathias Gerard, Ramon Da Fonseca, Paolo Massioni, and Eric Bideaux. Sliding mode observer for proton exchange membrane fuel cell: automotive application. *Journal of Power Sources*, 388:71–77, 2018.

[15] Jianxing Liu, Wensheng Luo, Xiaozhan Yang, and Ligang Wu. Robust model-based fault diagnosis for pem fuel cell air-feed system. *IEEE Transactions on Industrial Electronics*, 63(5):3261–3270, 2016.

[16] Christopher V Rao, James B Rawlings, and David Q Mayne. Constrained state estimation for nonlinear discrete-time systems: Stability and moving horizon approximations. *IEEE transactions on automatic control*, 48(2):246–258, 2003.

[17] M Böck, T Glück, W Kemmetmüller, A Kugi, and A Steinböck. Fortgeschrittene methoden der nichtlinearen regelung, 2014.

[18] José Manuel Andújar and Francisca Segura. Fuel cells: History and updating. a walk along two centuries. *Renewable and sustainable energy reviews*, 13(9):2309–2322, 2009.

[19] Omar Z Sharaf and Mehmet F Orhan. An overview of fuel cell technology: Fundamentals and applications. *Renewable and sustainable energy reviews*, 32:810–853, 2014.

[20] AJ Appleby. From sir william grove to today: fuel cells and the future. *Journal of Power Sources*, 29(1-2):3–11, 1990.

[21] Charles Stone and Anne E Morrison. From curiosity to "power to change the world®". *Solid State Ionics*, 152:1–13, 2002.

[22] Frano Barbir. *PEM fuel cells: theory and practice*. Academic press, 2012.

[23] Fengge Gao, Benjamin Blunier, and Abdellatif Miraoui. *Proton exchange membrane fuel cells modeling*. John Wiley & Sons, 2013.

[24] Ronald F Mann, John C Amphlett, Michael AI Hooper, Heidi M Jensen, Brant A Peppley, and Pierre R Roberge. Development and application of a generalised steady-state electrochemical model for a pem fuel cell. *Journal of power sources*, 86(1-2):173–180, 2000.

[25] Sang-Kyun Park and Song-Yul Choe. Dynamic modeling and analysis of a 20-cell pem fuel cell stack considering temperature and two-phase effects. *Journal of Power Sources*, 179(2):660–672, 2008.

[26] JH Lee, TR Lalk, and AJ Appleby. Modeling electrochemical performance in large scale proton exchange membrane fuel cell stacks. *Journal of power sources*, 70(2):258–268, 1998.

[27] Torsten Berning, DM Lu, and N Djilali. Three-dimensional computational analysis of transport phenomena in a pem fuel cell. *Journal of power sources*, 106(1-2):284–294, 2002.

[28] Thomas E Springer, TA Zawodzinski, and Shimshon Gottesfeld. Polymer electrolyte fuel cell model. *Journal of the electrochemical society*, 138(8):2334, 1991.

[29] John C Amphlett, Ronald F Mann, Brant A Peppley, Pierre R Roberge, and Aida Rodrigues. A model predicting transient responses of proton exchange membrane fuel cells. *Journal of Power sources*, 61(1-2):183–188, 1996.

[30] Dawn M Bernardi and Mark W Verbrugge. A mathematical model of the solid-polymer-electrolyte fuel cell. *Journal of the Electrochemical Society*, 139(9):2477, 1992.

[31] Jeferson M Correa, Felix A Farret, and Luciana Neves Canha. An analysis of the dynamic performance of proton exchange membrane fuel cells using an electrochemical model. In *IECON'01. 27th Annual Conference of the IEEE Industrial Electronics Society (Cat. No. 37243)*, volume 1, pages 141–146. IEEE, 2001.

[32] J Alejandro, Alicia Arce, and Carlos Bordons. Development and experimental validation of a pem fuel cell dynamic model. *Journal of power sources*, 173(1):310–324, 2007.

[33] Sandip Dutta, Sirivatch Shimpalee, and JW Van Zee. Numerical prediction of mass-exchange between cathode and anode channels in a pem fuel cell. *International Journal of Heat and Mass Transfer*, 44(11):2029–2042, 2001.

[34] John C Amphlett, Rob M Baumert, Ronald F Mann, Brant A Peppley, Pierre R Roberge, and Thomas J Harris. Performance modeling of the ballard mark iv solid polymer electrolyte fuel cell: I. mechanistic model development. *Journal of the Electrochemical Society*, 142(1):1, 1995.

[35] Lino Guzzella. Control oriented modeling of fuel-cell based vehicles. In *Presentation in NSF Workshop on the Integration of Modeling and Control for Automotive systems*. The University of Michigan US, 1999.

[36] Fred Daum. Nonlinear filters: beyond the kalman filter. *IEEE Aerospace and Electronic Systems Magazine*, 20(8):57–69, 2005.

[37] Niels Haverbeke. Efficient numerical methods for moving horizon estimation. *Diss., Katholieke Universiteit Leuven, Heverlee, Belgium*, 2011.

[38] AE Bryson and M Frazier. Smoothing for linear and nonlinear dynamic systems. In *Proceedings of the optimum system synthesis conference*, pages 353–364, 1963.

[39] Henry Cox. On the estimation of state variables and parameters for noisy dynamic systems. *IEEE Transactions on automatic control*, 9(1):5–12, 1964.

[40] Shi Shang Jang, Babu Joseph, and Hiro Mukai. Comparison of two approaches to on-line parameter and state estimation of nonlinear systems. *Industrial & Engineering Chemistry Process Design and Development*, 25(3):809–814, 1986.

[41] B Wayne Bequette. Nonlinear predictive control using multi-rate sampling. *The Canadian Journal of Chemical Engineering*, 69(1):136–143, 1991.

[42] Peter Klaus Findeisen. *Moving horizon state estimation of discrete time systems*. PhD thesis, University of Wisconsin–Madison, 1997.

[43] Christopher V Rao. *Moving horizon strategies for the constrained monitoring and control of nonlinear discrete-time systems*. The University of Wisconsin-Madison, 2000.

[44] Douglas G Robertson and Jay H Lee. A least squares formulation for state estimation. *Journal of process control*, 5(4):291–299, 1995.

[45] Douglas G Robertson, Jay H Lee, and James B Rawlings. A moving horizon-based approach for least-squares estimation. *AIChE Journal*, 42(8):2209–2224, 1996.

[46] Christopher V Rao, James B Rawlings, and Jay H Lee. Constrained linear state estimation—a moving horizon approach. *Automatica*, 37(10):1619–1628, 2001.

[47] Jürgen Adamy. *Nichtlineare Systeme und Regelungen*. Springer-Verlag, 2018.

[48] Devyani Varshney, Sachin C Patwardhan, Mani Bhushan, and Lorenz T Biegler. Batch and moving horizon estimation for systems subjected to non-additive stochastic disturbances. *IFAC-PapersOnLine*, 52(1):16–21, 2019.

[49] Sridhar Ungarala. Computing arrival cost parameters in moving horizon estimation using sampling based filters. *Journal of Process Control*, 19(9):1576–1588, 2009.

[50] Christopher V Rao and James B Rawlings. Constrained process monitoring: Moving-horizon approach. *AIChE journal*, 48(1):97–109, 2002.

[51] Eric L Haseltine and James B Rawlings. Critical evaluation of extended kalman filtering and moving-horizon estimation. *Industrial & engineering chemistry research*, 44(8):2451–2460, 2005.

[52] Eric A Wan and Rudolph Van Der Merwe. The unscented kalman filter for nonlinear estimation. In *Proceedings of the IEEE 2000 Adaptive Systems for Signal Processing, Communications, and Control Symposium (Cat. No. 00EX373)*, pages 153–158. Ieee, 2000.

[53] Rodrigo López-Negrete, Sachin C Patwardhan, and Lorenz T Biegler. Constrained particle filter approach to approximate the arrival cost in moving horizon estimation. *Journal of Process Control*, 21(6):909–919, 2011.